

## **Unravelling glacial hydroclimate in the Indo-Pacific Warm Pool: perspectives from water isotopes**

**Grace Windler<sup>1</sup>, Jessica E. Tierney<sup>1</sup>, Jiang Zhu<sup>2</sup>, and Christopher J. Poulsen<sup>2</sup>**

<sup>1</sup>Department of Geosciences, University of Arizona, Tucson, AZ, 85721, USA, <sup>2</sup>Department of Earth and Environmental Sciences, University of Michigan, Ann Arbor, MI, 48109, USA.

Corresponding author: Grace Windler ([gwindler@email.arizona.edu](mailto:gwindler@email.arizona.edu))

### **Key Points:**

- A new precipitation isotope record from southern Sumatra shows consistent enrichment during the five most recent glacial periods
- Glacial-interglacial changes in proxy precipitation isotope data from the Indo-Pacific Warm Pool agree well with isotope-enabled simulations
- Spatial heterogeneity of Warm Pool hydroclimate is linked to regional moisture convergence/divergence over the Pacific and Indian Oceans

This is the author manuscript accepted for publication and has undergone full peer review but has not been through the copyediting, typesetting, pagination and proofreading process, which may lead to differences between this version and the [Version of Record](#). Please cite this article as doi: [10.1029/2020PA003985](https://doi.org/10.1029/2020PA003985)

**Abstract**

The Indo-Pacific Warm Pool (IPWP) is home to the warmest sea surface temperatures in the world oceans, favoring strong tropospheric convection and heavy rainfall. The mechanisms controlling long-term change in the region's hydroclimate are still uncertain. Here, we present a 450,000-year record of precipitation  $\delta D$  from southern Sumatra that records a consistent pattern of glacial isotopic enrichment and interglacial depletion. We synthesize existing paleo-indicators of precipitation  $\delta D$  and  $\delta^{18}O$  in the IPWP and compare results with water isotope-enabled climate simulations of the Last Glacial Maximum (LGM). The simulations show glacial isotopic enrichment over the eastern Indian Ocean extending into the southern IPWP and isotopic depletion over southeast Asia, the west Pacific, and Australia. The pattern of simulated LGM isotopic change agrees generally well with our proxy synthesis. We conclude that reorganization of regional circulation under glacial conditions controls precipitation isotope variability in the IPWP: low-level tropospheric convergence dominates the signal in the north/east, whereas divergence controls the response in the south/west. Additional sensitivity simulations suggest that the LGM ice sheets and the associated lowering in sea level, rather than decreased greenhouse gases, are responsible for the distinctive spatial pattern in glacial changes of precipitation isotopes and hydroclimate across the IPWP.

**1 Introduction**

The Indo-Pacific Warm Pool (IPWP) has undergone extreme changes during glacial-interglacial cycles in the late Pleistocene. Changes in rainfall and large-scale modification of the landscape due to sea level fluctuations altered the biogeography across the Sunda Shelf and

reorganized ocean and atmosphere circulation in the region (Bird et al., 2005; DiNezio et al., 2016; Heaney, 1991). During the Last Glacial Maximum (LGM; 23-19 ka), evidence of cooler and drier conditions across much of the IPWP has been found in terrestrial records, including pollen, charcoal, dust, terrestrial sediments, various stable carbon isotope records, and geomorphic features (Bird et al., 2005; DiNezio & Tierney, 2013; Reeves et al., 2013).

Stable isotopes of precipitation ( $\delta D_{\text{precip}}$ ,  $\delta^{18}O_{\text{precip}}$ ) can be powerful tools for understanding hydroclimate variations, if the mechanisms driving isotopic values of rainfall are understood. Many tropical paleoclimate studies have associated changes in  $\delta D_{\text{precip}}$  or  $\delta^{18}O_{\text{precip}}$  with precipitation amount, on the basis of the observed inverse relationship between precipitation amount and its isotopic composition (Clark & Fritz, 1997; Dansgaard, 1964; Rozanski et al., 1993). Interpreting the decrease in IPWP  $\delta D_{\text{precip}}$  values during the LGM as an increase in precipitation amount, following the classic amount effect, is difficult to reconcile with proxy evidence of widespread regional aridity (Ayliffe et al., 2013; Konecky et al., 2016; Niedermeyer et al., 2014; Wicaksono et al., 2017). However, recent research has found that moisture transport/circulation (Aggarwal et al., 2012; Moore et al., 2014) and cloud type (convective vs. stratiform) (Aggarwal et al., 2016; Kurita, 2013) are also important controls on precipitation isotopes, complicating interpretations of paleo archives such as leaf waxes or speleothems. Modern water isotope studies in the IPWP hint at a more complex view of regional precipitation isotopes than the amount effect and emphasize the importance of multiple processes, including strength of regional convection, rain re-evaporation, cloud types, and seasonally changing

moisture source pathways (Aldrian & Susanto, 2003; Belgaman et al., 2017; Cobb et al., 2007; Griffiths et al., 2009; Konecky et al., 2016, 2019; Kurita et al., 2009; Moerman et al., 2013; Wurtzel et al., 2018)..

Here, we aim to clarify the relationship between precipitation isotopes and glacial climate in the IPWP using both proxy and model information. To improve both the spatial and temporal coverage in the southern IPWP, we present a new leaf wax-derived  $\delta D_{\text{precip}}$  record from core MD98-2152 off southwest Sumatra (Figure 1), which extends to 450 ka, spanning the five most recent glacial periods. To understand the mechanisms influencing rainfall isotopes over these glacial – interglacial timescales, we focus specifically on the LGM as there is an abundance of proxy data available for that time (Figure 1). We directly compare proxy  $\delta D_{\text{precip}}$  changes during the LGM to those in isotope-enabled model simulations conducted with the Community Earth System Model to diagnose how the glacial climate state influences isotopic variability across the IPWP.

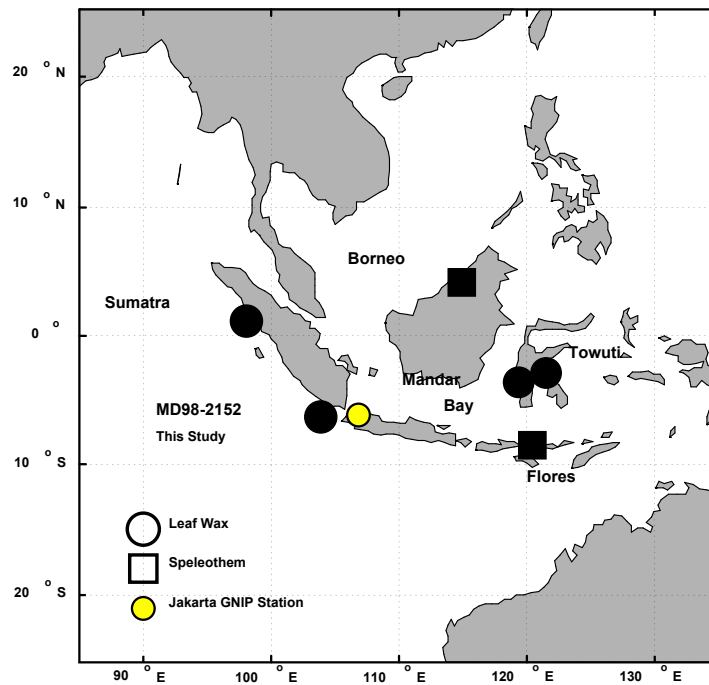


**Figure 1.** Locations of proxy sites discussed in this text: speleothem  $\delta^{18}\text{O}$  from Borneo (Partin et al., 2007), leaf wax  $\delta\text{D}$  from northwest Sumatra (Niedermeyer et al., 2014), leaf wax  $\delta\text{D}$  from Lake Towuti (Konecky et al., 2016), leaf wax  $\delta\text{D}$  from Mandar Bay (Wicaksono et al., 2017), leaf wax  $\delta\text{D}$  from southern Sumatra (this study), and speleothem  $\delta^{18}\text{O}$  from Flores (Ayliffe et al., 2013). Yellow circle represents the Jakarta GNIP station (section 2.2).

## 2 Background

### 2.1 Modern seasonality of rainfall and isotopes in the IPWP

The southern sector of the IPWP has more pronounced rainfall seasonality than the northern sector (Aldrian & Susanto, 2003; Dubois et al., 2014). From December to March (DJFM), the northwest monsoon brings heavy rainfall to southern Sumatra, Java, and Flores. From June to September (JJAS), winds are reversed and the southeast monsoon moves the loci of precipitation north of the equator, decreasing rainfall across the southern IPWP (Aldrian &

Susanto, 2003; Schott & McCreary, 2001). By contrast, much of the northern IPWP experiences heavy rainfall year round (Aldrian & Susanto, 2003; Moerman et al., 2013).

Likewise, the northern and southern IPWP exhibit distinct  $\delta D_{\text{precip}}$  and  $\delta^{18}O_{\text{precip}}$  values. In northern Borneo, for example, where there is little seasonality in rainfall amount, the seasonal  $\delta^{18}O_{\text{precip}}$  reflects regional convection and shifts in moisture sources between the South China Sea and Java Sea (Cobb et al., 2007; Moerman et al., 2013). Similarly, rainfall in northwest Sumatra does not exhibit pronounced seasonality and is largely sourced locally from the Indian Ocean (Niedermeyer et al., 2014; Wu et al., 2009; Wurtzel et al., 2018). Precipitation isotope variability over this area reflects changes in moisture source and rainfall amount, with the most depleted values associated with a local Indian Ocean source (Belgaman et al., 2017; Wurtzel et al., 2018). In the southern IPWP, where rainfall is more seasonal, there is an increased regional amount effect during the dry season. For instance, at Lake Towuti  $\delta^{18}O_{\text{precip}}$  and  $\delta D_{\text{precip}}$  during the dry season has a significant relationship with the amount of rainfall, whereas northwesterly rainfall during the wet season does not vary with amount and instead reflects regional convection (Konecky et al., 2016). A similar seasonal contrast in source and isotopic signature of rainfall has been observed in Flores (Griffiths et al., 2009), the most southerly site discussed in this paper.

## **2.2 Examining monthly rainfall isotopes near MD98-2152**

To understand how the isotopic composition of regional rainfall over MD98-2152 (Figure 1) varies with the amount and source of precipitation, we use modern observations from the nearest Global Network of Isotopes in Precipitation (GNIP) monitoring station in Jakarta

(6.18°S, 106.83°E), approximately 300 km away. The station discontinuously recorded monthly data from 1962 – 1998 (IAEA/WMO, 2019). Seasonally variable rainfall amount at Jakarta reflects a DJFM wet season associated with the northwest monsoon and a JJAS dry season associated with the southeast monsoon (Figure 2a). Here we use “wet” and “dry” to describe the relative amount of precipitation between seasons. The  $\delta D_{\text{precip}}$  (Figure 2a) and  $\delta^{18}O_{\text{precip}}$  (not shown) mimic the seasonal changes in rainfall amount; DJFM precipitation is up to ~20‰ more depleted than JJAS  $\delta D_{\text{precip}}$ .

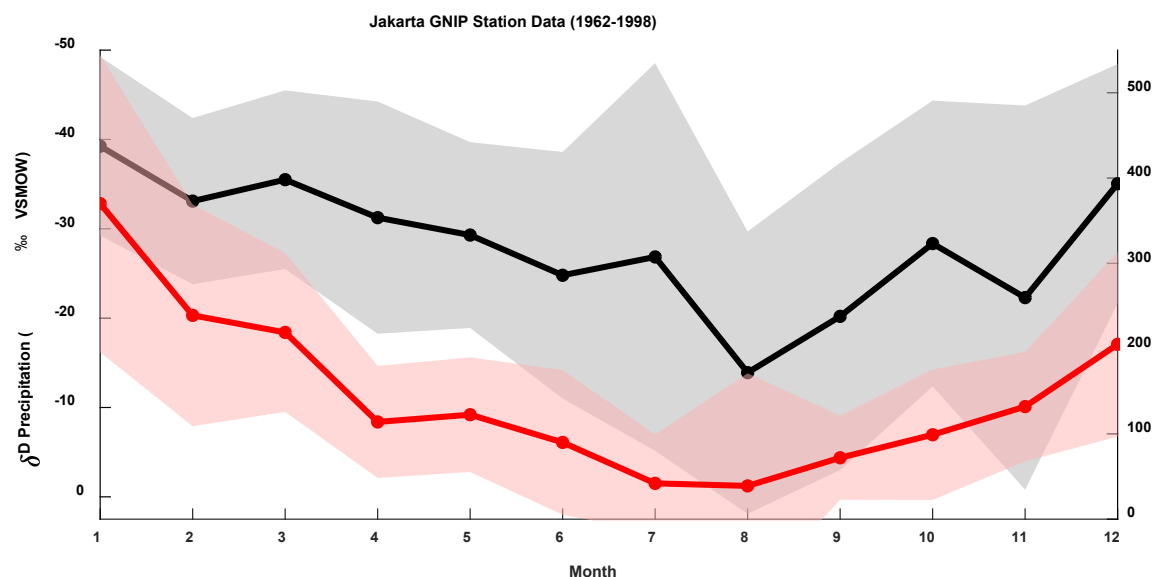


**Figure 2.** a) Monthly precipitation and  $\delta D_{\text{precip}}$  values recorded at the Jakarta GNIP station, over the period 1962 – 1998 (IAEA/WMO, 2019). Solid lines represent median of the monthly data. Shading represents  $1\sigma$  error. Note the reversed left y-axis. b) HYSPLIT4 back trajectories for rainy days in Jakarta during the months of December – March (wet season) when GNIP data are available (280 trajectories plotted for 70 rainy days). Each black line represents a single 96-hour trajectory ending at the Jakarta GNIP station (yellow circle). c) Same as in panel b, but for the months of June – September (180 trajectories plotted for 45 rainy days).



We compare the Jakarta GNIP data with backward trajectories of likely rain-bearing air parcels from the Hybrid Single Particle Lagrangian Integrated Trajectory (HYSPLIT4) model (Draxler, 1999) using the NCEP/NCAR Reanalysis V2 gridded dataset (available here: <http://www.esrl.noaa.gov/psd/>). Rainy days that occurred during the months with Jakarta GNIP measurements were identified using the Global Historical Climate Network-Daily (GHCN-D) observations from the same location (<http://www.ncdc.noaa.gov/ghcn-daily-description>) (Menne et al., 2012). Starting at Jakarta, using HYSPLIT4, we calculated 4-day (96 hours) back trajectories of air masses at ~850 hPa at 6-hour intervals for rainy days. The back trajectories show a strong seasonal difference in potential source areas and pathways corresponding to seasonal changes in monsoon winds (Figure 2b, 2c). During DJFM, when Jakarta precipitation is greatest and most isotopically depleted (Figure 2a), air masses mostly travel from the South China Sea and equatorial east Indian Ocean (Figure 2b). During JJAS, when Jakarta precipitation is smallest and most enriched (Figure 2a), air masses track from the Timor Sea and Indian Ocean to the southeast (Figure 2c).

### **2.3 Leaf wax reconstructions of hydroclimate variability**

The wax layer of higher terrestrial plant leaves consists largely of long chain ( $>C_{25}$ ) *n*-alkanes and *n*-alkanoic acids (Eglinton & Hamilton, 1967). These waxes are geologically stable, accumulating in marine and lacustrine sediments via runoff or wind (Eglinton & Eglinton, 2008). The  $\delta D$  of leaf waxes ( $\delta D_{\text{wax}}$ ) reflects the variability of source water used by plants, which is controlled by the  $\delta D$  of regional precipitation ( $\delta D_{\text{precip}}$ ) with an apparent offset. The offset

between  $\delta D_{\text{precip}}$  and  $\delta D_{\text{wax}}$  ( $\epsilon_{\text{water-wax}}$ ) varies among different plant types and photosynthetic pathways (Sachse et al., 2012). Specifically, monocots (grasses) synthesize waxes that are more depleted relative to precipitation (larger  $\epsilon_{\text{water-wax}}$ ) than other vascular plants, possibly due to physiological differences in evapotranspiration rates from the leaves and/or the rate and seasonal timing of leaf wax synthesis (Gao et al., 2014; Sachse et al., 2012). Grasses with different photosynthetic pathways also exhibit different  $\epsilon_{\text{water-wax}}$ . Specifically,  $C_3$  grasses synthesize more depleted waxes relative to precipitation than  $C_4$  grasses (Gao et al., 2014; Sachse et al., 2012); however, grasses are predominantly  $C_4$  in the IPWP, so regional vegetation is a mix of  $C_3$  dicots (smaller  $\epsilon_{\text{water-wax}}$ ) and  $C_4$  grasses (larger  $\epsilon_{\text{water-wax}}$ ). The  $\delta D_{\text{wax}}$  from sediments have been used previously for hydroclimate reconstruction across the IPWP over various time scales (Konecky et al., 2016; Niedermeyer et al., 2014; Tierney et al., 2010, 2012; Wicaksono et al., 2017) and commonly used in tandem with  $\delta^{13}C_{\text{wax}}$  measurements to correct for the impact of vegetation change ( $C_3$  dicots vs.  $C_4$  grasses) on  $\delta D_{\text{wax}}$ . Here, we use this approach to reconstruct  $\delta D_{\text{precip}}$  for the last 450 kyr from leaf waxes deposited in marine sediments from the Sumatran margin.

### 3 Materials and Methods

#### 3.1 Site MD98-2152 and $\delta D_{\text{wax}}$ analysis

MD98-2152 (6.33°S, 103.88°E) was recovered from a water depth of 1796 m and is approximately 30.5 m long. Details regarding the age model for MD98-2152 have been previously described by Windler et al. (2019). Briefly, two radiocarbon dates near the top of the core constrain the age-depth relationship spanning the LGM. Tie points between  $\delta^{18}O$  of *G.*

*ruber* from the sediment core and the global benthic  $\delta^{18}\text{O}$  stack (Lisiecki & Raymo, 2005) were used in conjunction with the radiocarbon dates as inputs to OxCal version 4.3 (Bronk Ramsey, 2008) to generate the age model. The average sample resolution downcore is  $\sim 2.5$  kyr, with the highest resolution between 450 – 370 ka and 30 – 1 ka.

Purification of leaf wax fatty acids in samples from marine core MD98-2152 was also described by Windler et al. (2019). Briefly, organic material was extracted from freeze-dried sediment samples using an Accelerated Solvent Extractor with a 9:1 (v/v) mixture of dichloromethane:methanol. Leaf waxes were isolated from each total lipid extract using column chromatography with  $\text{NH}_2$  as the solid phase. Each sample was methylated with methanol of a known isotopic composition to form fatty acid methyl esters (FAMES) and further purified via a final column chromatography step using silica gel.

Higher chain ( $\geq \text{C}_{28}$ ) fatty acids are suggested to be most representative of terrestrial vascular plants (Kusch et al., 2010); however, algal contributions have been detected for fatty acid chain lengths as high as  $\text{C}_{28}$  (Feakins et al., 2007; Volkman et al., 1980). Here, we measure the  $\text{C}_{30}$  fatty acid to avoid contamination from aquatic plant material. The hydrogen isotopic composition of the  $\text{C}_{30}$  fatty acid was measured in each sample using a gas chromatography-isotope ratio-monitoring mass spectrometer (GC-IR-MS; Thermo Delta V Plus). All  $\delta\text{D}$  values are reported in ‰ vs. Vienna Standard Mean Ocean Water (VSMOW). Samples were run at least in duplicate ( $\sim 30\%$  were run in triplicate). External FAME and *n*-alkane standards of known isotopic composition were run every five injections to monitor drift and ensure accuracy.

Precision of the  $\delta D_{wax}$  measurements was assessed to be  $\pm 1.5\text{‰}$  ( $1\sigma$ ).  $\delta D_{wax}$  measurements were corrected for the isotopic composition of the added methyl group during the methylation process via mass balance. Some samples lacked enough  $C_{30}$  fatty acid material for reliable duplicate analyses, resulting in missing data points in our time series, mainly between  $\sim 42 - 30$  ka.

### 3.2 Vegetation correction

The carbon isotopic composition of leaf waxes ( $\delta^{13}C_{wax}$ ) in MD98-2152 indicate shifts between predominantly  $C_3$  vegetation during interglacial periods and a larger proportion of  $C_4$  grasses during glacial periods (Windler et al., 2019); therefore, the varying  $\epsilon_{water-wax}$  must be accounted for when calculating  $\delta D_{precip}$  from  $\delta D_{wax}$  at this location through time. We apply a Bayesian method that has been successfully used in other paleo-rainfall studies to calculate  $\delta D_{precip}$  (Bhattacharya et al., 2018; Tierney et al., 2017). We use paired  $\delta^{13}C_{wax}$  measurements from MD98-2152 to estimate the fraction of  $C_4$  plant contribution of leaf waxes in each sample ( $f_{C4}$ ), based on designated endmember  $\delta^{13}C_{C4}$  and  $\delta^{13}C_{C3}$  values as described by Tierney et al. (2017). Estimated  $f_{C4}$  is used in conjunction with designated endmember  $\epsilon_{C4}$  and  $\epsilon_{C3}$  values to calculate a vegetation-weighted  $\epsilon_{water-wax}$  for each sample (Equation 1), which is then used to calculate  $\delta D_{precip}$  (Equation 2):

$$\epsilon_{water-wax} = f_{C4} \times \epsilon_{C4} + (1 - f_{C4}) \times \epsilon_{C3} \quad (1)$$

$$\delta D_{precip} = \frac{1000 + \delta D_{wax}}{\left(\frac{\epsilon_{water-wax}}{1000}\right) + 1} - 1000 \quad (2)$$

We use  $C_4$  endmember values ( $\pm$  standard error) from Sachse et al. (2012):  $\delta^{13}C_{C_4} = -20.7 \pm 0.7\text{‰}$  and  $\epsilon_{C_4} = -132 \pm 3.3\text{‰}$  (monocots only). To represent tropical  $C_3$  plants we use the endmember  $\delta^{13}C_{C_3} = -33.4 \pm 0.4\text{‰}$  (standard error) from the “All Africa” dataset (Garcin et al., 2014). We use  $\epsilon_{C_3}$  endmember values available in Sachse et al. (2012), excluding  $C_3$  grasses:  $\epsilon_{C_3} = -114 \pm 2.1\text{‰}$  (standard error). We note that all endmember values correspond to  $C_{29}$   $n$ -alkane  $\delta^{13}C$  and  $\epsilon_{\text{water-wax}}$  because comparable data does not exist for  $C_{30}$   $n$ -acid. While it is unknown how different apparent fractionation is between  $C_{29}$   $n$ -alkanes and  $C_{30}$   $n$ -acids (Sachse et al., 2012), they appear to be closely related (Gao et al., 2014); therefore, we assume they are equivalent.

### 3.3 iCESM simulations

Model simulations of the LGM and pre-industrial (PI) were conducted with the isotope-enabled Community Earth System Model Version 1.2 (iCESM) (Brady et al., 2019). Descriptions of the individual components of iCESM, including the atmosphere (iCAM5), ocean (iPOP2), and land (iCLM4) models can be found in Nusbaumer et al. (2017), Wong et al. (2017), and Zhang et al. (2017), respectively. CESM1 is fully coupled and has been shown to simulate a realistic modern climate state in the tropics as well as patterns of rainfall and SST change for the LGM that are consistent with paleo proxy data in the IPWP (Brady et al., 2019; DiNezio et al., 2016, 2018; Thirumalai et al., 2019; Zhu et al., 2017). Among multiple isotope-enabled models, iCESM (with iCAM5) has been found to be one of the better models at realistically simulating the observed  $\delta^{18}O_{\text{precip}}$  variability in convective systems (Hu et al., 2018), which is critical for the

simulation of tropical isotopic changes since the LGM (Jasechko et al., 2015). For this reason, iCESM may be especially well suited for studying glacial-interglacial changes in water isotopes and hydroclimate.

The PI and LGM simulations were described in Tierney et al. (2020). The PI simulation was run for 900 years with constant climate forcings set at 1850 C.E. values. The LGM simulation was also run for 900 years and used prescribed boundary conditions consistent with the Paleoclimate Modelling Intercomparison Project version 4 protocols (PMIP4; Kageyama et al., 2017), including altered Earth orbital parameters, reduced greenhouse gas (GHG) concentrations, and changes in surface albedo, topography, and land-sea distribution associated with LGM ice sheets. A constant value of 1.05‰ was added to the  $\delta^{18}\text{O}$  (~8‰ to  $\delta\text{D}$ ) of ocean water in the LGM simulation to account for seawater enrichment from the global ice volume effect (Duplessy et al., 2002). Additional sensitivity experiments were conducted by implementing one LGM climate forcing at a time to isolate the different impacts of GHGs and ice sheets (ICE). Specifically, in the GHG experiment, GHG concentrations in the PI simulation were reduced to LGM levels with all other boundary conditions held constant. Likewise, in the ICE experiment, the LGM ice sheet forcing was added with all other boundary conditions held at PI values. Both sensitivity experiments were branched from the PI climate state and run for an additional 150 years. Although these sensitivity experiments were not in an equilibrium state, they were integrated long enough to capture major features of the tropical hydroclimate responses to external forcings (DiNezio et al., 2016).

To evaluate the performance of iCESM in simulating the seasonal hydroclimate cycle at our study site, we compare the Jakarta GNIP observations with model results in the isotope-enabled Last Millennium Ensemble (Brady et al., 2019; Stevenson et al., 2019). The simulated monthly precipitation for the grid cell containing Jakarta matches well with GNIP observations from 1962 – 1998 (Figure 3a). The simulated  $\delta D_{\text{precip}}$  cycle also resembles that in the Jakarta GNIP observations, but the values are more depleted than the observational median with the greatest difference spanning the DJFM wet season (Figure 3b). These results suggest that iCESM realistically captures seasonal hydroclimate variability at our study site, although the modeled  $\delta D_{\text{precip}}$  are biased toward more depleted values.

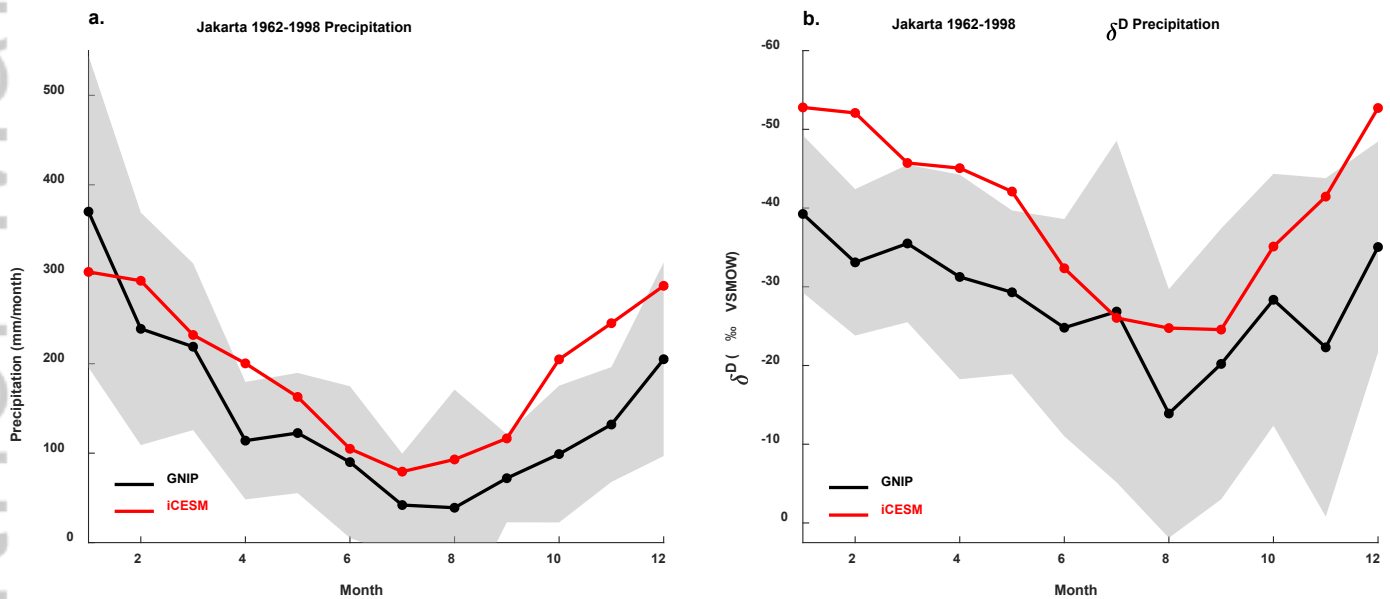


**Figure 3.** a) Monthly precipitation cycle for Jakarta GNIP observations (black) and iCESM Last Millennium Ensemble simulation (red) for the period 1962-1998. Simulated values were taken

from grid cell overlying Jakarta GNIP station (6.63°S, 107.5°E). Solid black line represents median GNIP observations and shading indicates  $1\sigma$  error. b) Same as in panel a, but for  $\delta D_{\text{precip}}$ .

### 3.4 Proxy data comparison and temperature correction

In addition to the new southern Sumatra  $\delta D_{\text{precip}}$  record presented here, we calculate the magnitude of LGM (23 – 19 ka) to LH (4 – 0 ka) changes recorded in five published records of paleo-precipitation isotopes from across the IPWP (Figure 1). Changes were calculated for each location by subtracting the mean values for the listed time intervals. We use  $\delta D_{\text{wax}}$  and  $\delta^{13}\text{C}_{\text{wax}}$  measurements from northwest Sumatra (Niedermeyer et al., 2014), Lake Towuti (Konecky et al., 2016; Russell et al., 2014), and Mandar Bay (Wicaksono et al., 2017) to calculate  $\delta D_{\text{precip}}$  using the same vegetation correction method described above (see Methods section 3.2). For samples with missing  $\delta^{13}\text{C}_{\text{wax}}$  measurements, we employed linear interpolation between points.

Since  $\delta D_{\text{precip}}$  from MD98-2152 includes the five most recent glacial periods and the LGM is not particularly well-resolved (Figure 4a), we calculate an average glacial – interglacial change to compare with other proxy locations and model simulations. First, we define glacial (interglacial) periods based on the timing of the Marine Isotope Stage (MIS) during which the global benthic stack is most enriched (depleted) for each glacial cycle included in the record (Figure 4b; Lisiecki and Raymo, 2005). Specifically, we define glacial periods as MIS 2 (23 – 19 ka), MIS 6 (149 – 137 ka), MIS 8 (262 – 242 ka), MIS 10 (346 – 335 ka), and MIS 12 (436 – 428 ka). Likewise, interglacial periods are defined as the Late Holocene (4 – 0 ka), MIS 5 (124 – 109 ka), MIS 7 (215 – 203 ka and 241 – 235 ka), MIS 9 (327 – 315 ka), and MIS 11 (404 – 396 ka).



We then subtracted the average of MD98-2152  $\delta D_{\text{precip}}$  during the listed interglacials from the average during the listed glacials, the result of which is reported below in Table 1.

Since the  $\delta^{18}\text{O}$  of speleothem calcite is a function of cave temperature, we correct the speleothem records from Borneo and Flores accordingly to account for the effect of LGM cooling. This correction assumes that changes in cave temperature follow changes in mean annual surface temperature. To estimate the magnitude of mean annual temperature change, we use the simulated change in iCESM from the nearest grid cell to each location:  $\Delta T = -4.5^\circ\text{C}$  in northern Borneo and  $\Delta T = -3.2^\circ\text{C}$  in Flores (Figure 5c). We then correct the  $\delta^{18}\text{O}$  values at each location for the contribution due to temperature, which has been found to change by 0.2‰ per  $^\circ\text{C}$  (Kim & O’Neil, 1997), using the following equation:

$$\text{Corrected } \Delta\delta^{18}\text{O} = \Delta\delta^{18}\text{O} - |\Delta T| \times 0.2 \quad (3)$$

For consistency with  $\delta D_{\text{wax}}$  and model data, we also converted changes in speleothem values originally reported in Vienna Pee Dee Belemnite (VPDB) to VSMOW values using the following equation (Clark & Fritz, 1997; Coplen et al., 1983):

$$\delta^{18}\text{O}_{\text{VSMOW}} = 1.03091 \times \delta^{18}\text{O}_{\text{VPDB}} + 30.91 \quad (4)$$

We do not correct any of the proxy records discussed in this study for the +1.05‰  $\delta^{18}\text{O}$  (~8‰  $\delta D$ ) enrichment of seawater from increased global ice volume during glacial periods (Duplessy et al., 2002). The seawater enrichment is included in the LGM simulations; therefore, to ensure a direct comparison, the global ice volume signal must be included in the proxy data.

## 4 Results

### 4.1 MD98-2152 leaf wax record

The vegetation effect on  $\epsilon_{\text{water-wax}}$  is greatest during glacial periods, such as MIS 2 (23 – 19 ka), MIS 6 (149 – 137 ka), or MIS 8 (262 – 242 ka), when relatively larger fractions of C<sub>4</sub> grasses contributed leaf waxes from southern Sumatra and western Java (Figure S1); therefore, glacial enrichment of  $\delta D_{\text{precip}}$  was more pronounced than is indicated by the uncorrected  $\delta D_{\text{wax, record}}$ . The vegetation corrected  $\delta D_{\text{precip}}$  data from MD98-2152 ranges from -43.2‰ to -15.5‰ (Figure 4a).  $\delta D_{\text{precip}}$  regularly approaches values of -35 to -40‰ during interglacial periods, including the Late Holocene and MIS 5, 7, 9, and 11 (Figure 4a). Glacial  $\delta D_{\text{precip}}$  values regularly approach -20 to -25‰, including MIS 2, 6, 8, 10, and 12 (Figure 4a). Overall, the  $\delta D_{\text{precip}}$  from MD98-2152 closely tracks glacial – interglacial cycles observed in the global benthic foraminifera  $\delta^{18}\text{O}$  stack (Lisiecki & Raymo, 2005) for the last 450 kyr (Figure 4b). The LGM appears less enriched in  $\delta D$  than previous glacial periods (Figure 4a); however, uncertainties in our age model and the interval of missing values directly prior to the LGM may mean that the full extent of enrichment is not realized in this record.

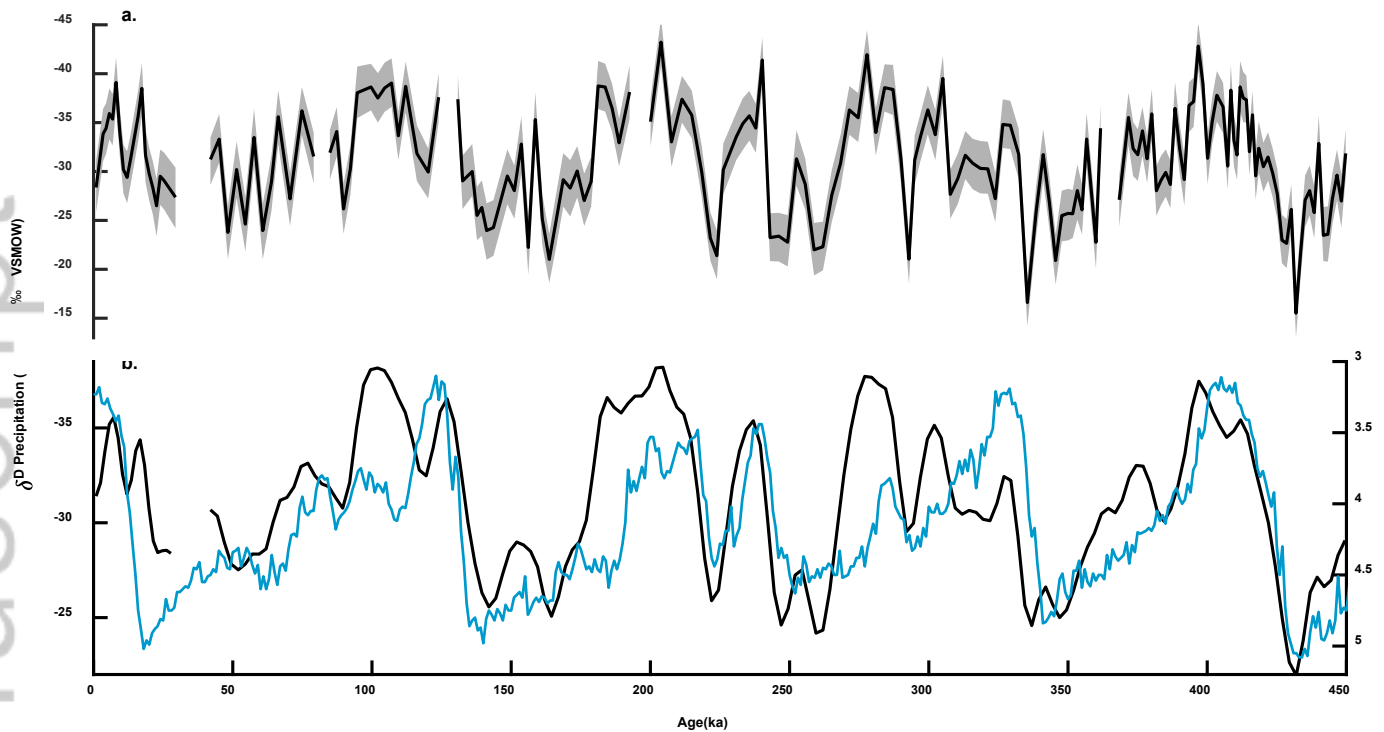


**Figure 4.** a) The  $\delta D_{\text{precip}}$  record calculated from  $\delta D_{\text{wax}}$  and  $\delta^{13}\text{C}_{\text{wax}}$  from marine core MD98-2152 (black). Shaded area represents 1 $\sigma$  error. b) A Gaussian smoothed version of the  $\delta D_{\text{precip}}$  record (black) plotted with the global benthic foraminifera  $\delta^{18}\text{O}$  stack (light blue) (Lisiecki & Raymo, 2005).

## 4.2 iCESM simulations

Simulated mean annual LGM-PI changes in the IPWP indicate that during glacial conditions the entire region was cooler by  $\sim 3\text{--}6^\circ\text{C}$  (Figure 5c) and more arid (reduced precipitation), with the greatest drying concentrated over the southern IPWP and extending into the tropical eastern Indian Ocean (Figure 5a). LGM-PI changes in mean annual precipitation-weighted  $\delta D_{\text{precip}}$  show a distinctive spatial pattern, with rainfall becoming more enriched over the Indian Ocean, but more depleted over the Pacific (Figure 5b). Differences in surface ocean

$\delta D$  show three distinct regional patterns: an enriched eastern Indian Ocean, a less-enriched western Pacific, and a least-enriched South China Sea (Figure 5d).

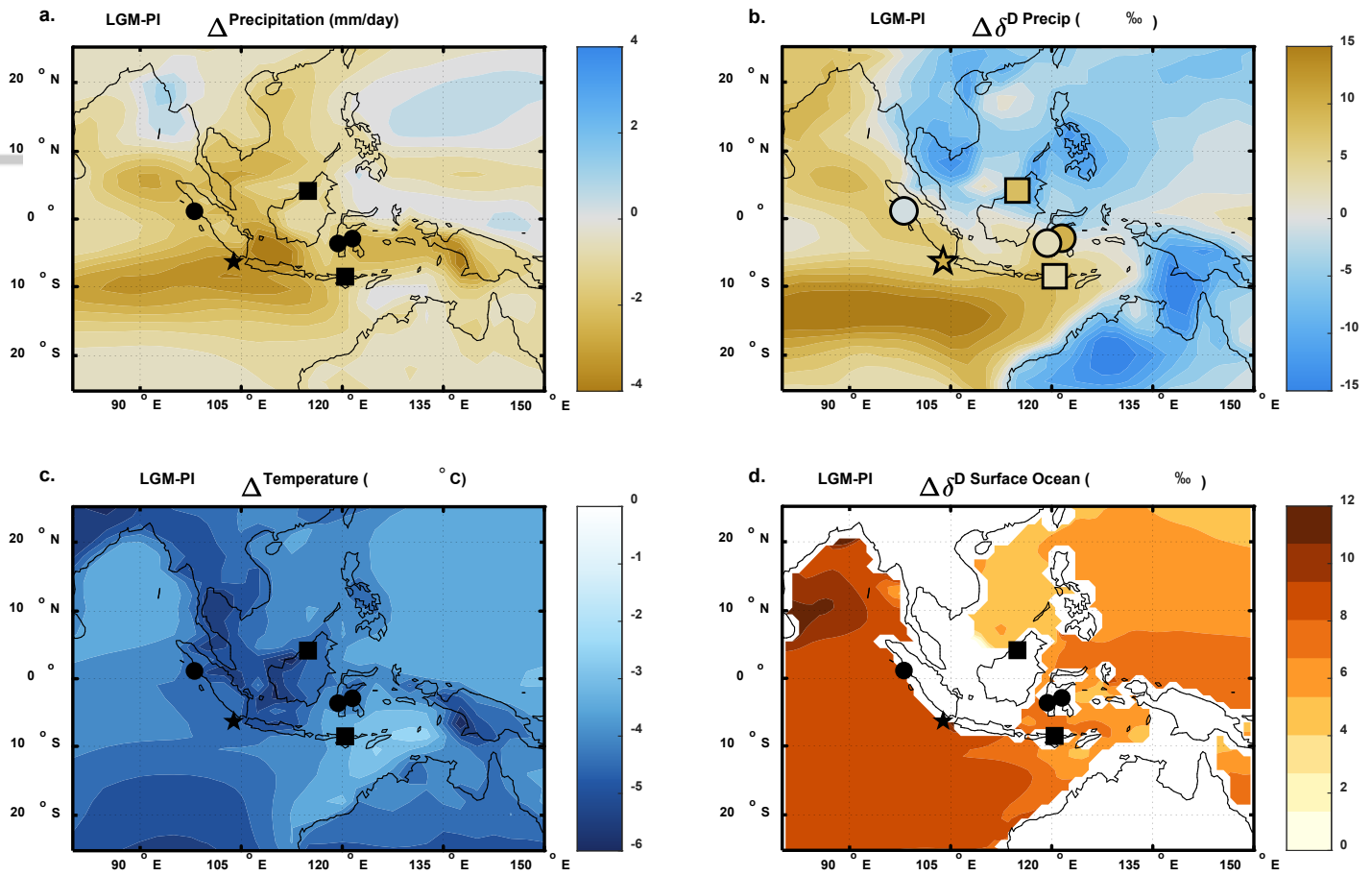


**Figure 5.** Simulated mean annual LGM-PI changes in a) total precipitation, b)  $\delta D_{\text{precip}}$  (weighted by precipitation amount), c) surface temperature, and d)  $\delta D$  of the surface ocean. Shapes indicate locations of proxy sites listed in Figure 1. Filled shapes in panel b show the calculated LGM (23 – 19 ka) to LH (4 – 0 ka) isotopic change recorded by either sedimentary leaf waxes (circles) or speleothems (squares). The star represents MD98-2152 (value is average glacial-interglacial change; see section 3.5). Speleothem data in panel b are temperature corrected based on nearest grid cell in panel c (see section 3.4). All  $\delta D$  values are reported in VSMOW.

Simulated seasonal LGM-PI changes in  $\delta D_{\text{precip}}$  show that DJFM (northwest monsoon) rainfall exhibits a similar pattern of isotopic change to that of the annual average: depleted rainfall over the west Pacific extends across  $\sim 0 - 5^{\circ}\text{S}$  into the Indian Ocean and enriched rainfall is concentrated in the Indian Ocean over the Bay of Bengal and  $10 - 20^{\circ}\text{S}$  (Figure 6a). Precipitation across the Sunda Shelf decreases during DJFM, with the greatest reduction concentrated south of Java and north of the shelf, between Malaysia and Borneo (Figure 7a). Conversely, JJAS (southeast monsoon) rainfall is enriched in  $\delta D$  south of the equator, with the greatest enrichment concentrated between roughly  $0 - 10^{\circ}\text{S}$ , including the tropical eastern Indian Ocean and southern IPWP (Figure 6b). This band of greatest JJAS enrichment is matched by a decrease in JJAS rainfall across the same region (Figure 7b). Maximum rainfall reduction during DJFM is approximately -4 mm/day across Java and the Lesser Sunda Islands (Figure 7a), whereas change in JJAS rainfall reaches -6 mm/day over the same region (Figure 7b), which translates to a  $\leq 40\%$  decrease during DJFM and an approximately 70% decrease during JJAS (% change not shown).

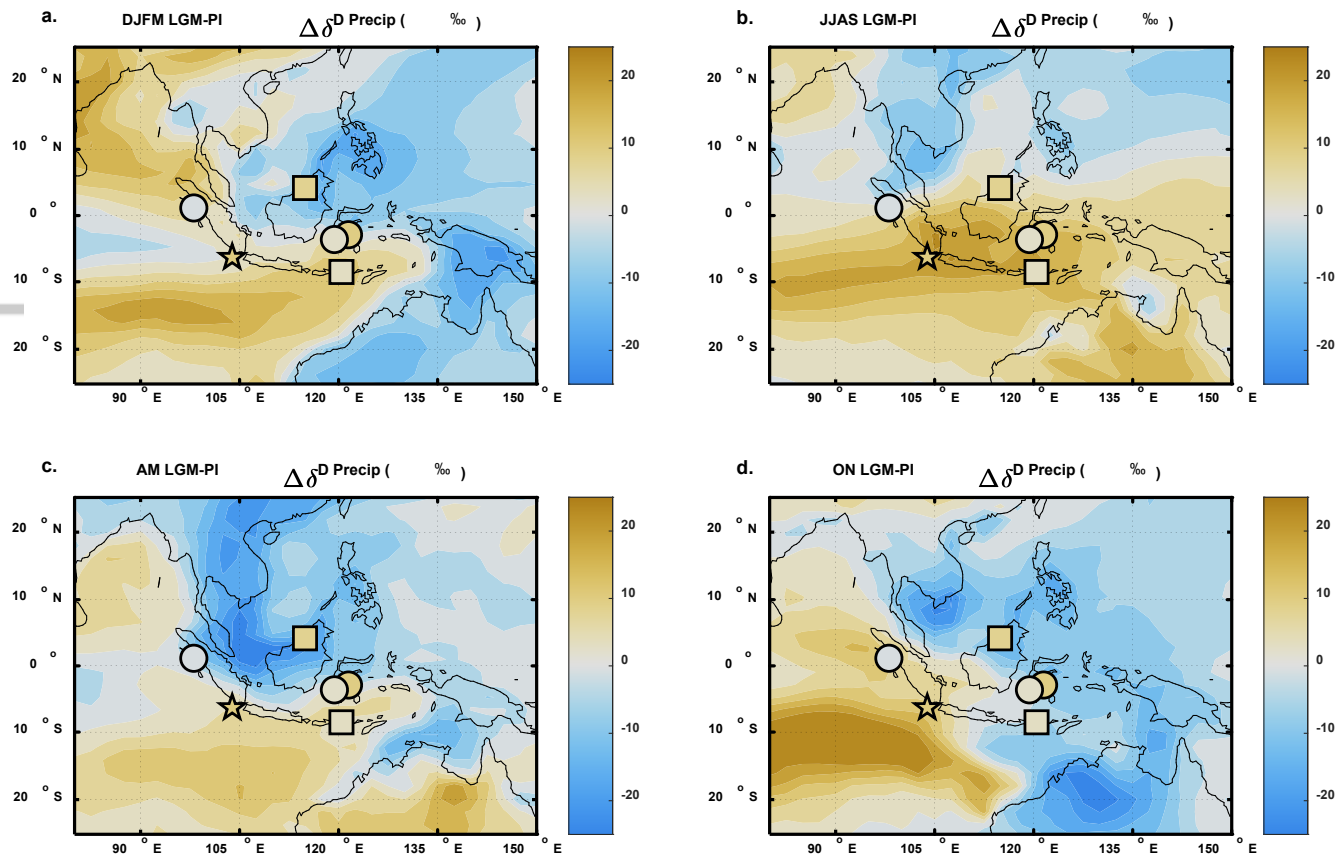


**Figure 6.** Simulated seasonal LGM-PI changes in  $\delta D_{\text{precip}}$  for a) December – March (DJFM), b) June – September (JJAS), and the transitional months c) April – May (AM) and d) October – November (ON). DJFM corresponds to the southern IPWP wet season and JJAS corresponds to the dry season. Filled shapes mark the locations of proxy sites and their calculated isotopic change between the LGM (23 – 19 ka) and LH (4 – 0 ka). All isotope values are reported in VSMOW. Speleothem data are temperature corrected.

The transitional months of April – May (AM) and October – November (ON) also show the distinct spatial pattern of isotopic change:  $\delta D$  depletion over the western Pacific and enrichment over the eastern Indian Ocean (Figure 6c, 6d), but the centers of greatest depletion and enrichment vary. Precipitation changes during AM somewhat mirror the pattern of change in

$\delta D_{\text{precip}}$ , with simulated increases in precipitation over the Andaman Sea and southeast Asia and drying to the south (Figure 7c); however, the largest reduction in rainfall over the Sahul Shelf at 10°S (Figure 7c) corresponds to a center of depleted rainfall rather than enrichment (Figure 6c). Simulated changes in ON precipitation show widespread drying over southeast Asia, the Indian Ocean, and Australia (Figure 7d). The most severe drying during ON is concentrated over southern Sumatra and western Java and extends across the tropical eastern Indian Ocean (Figure 7d).

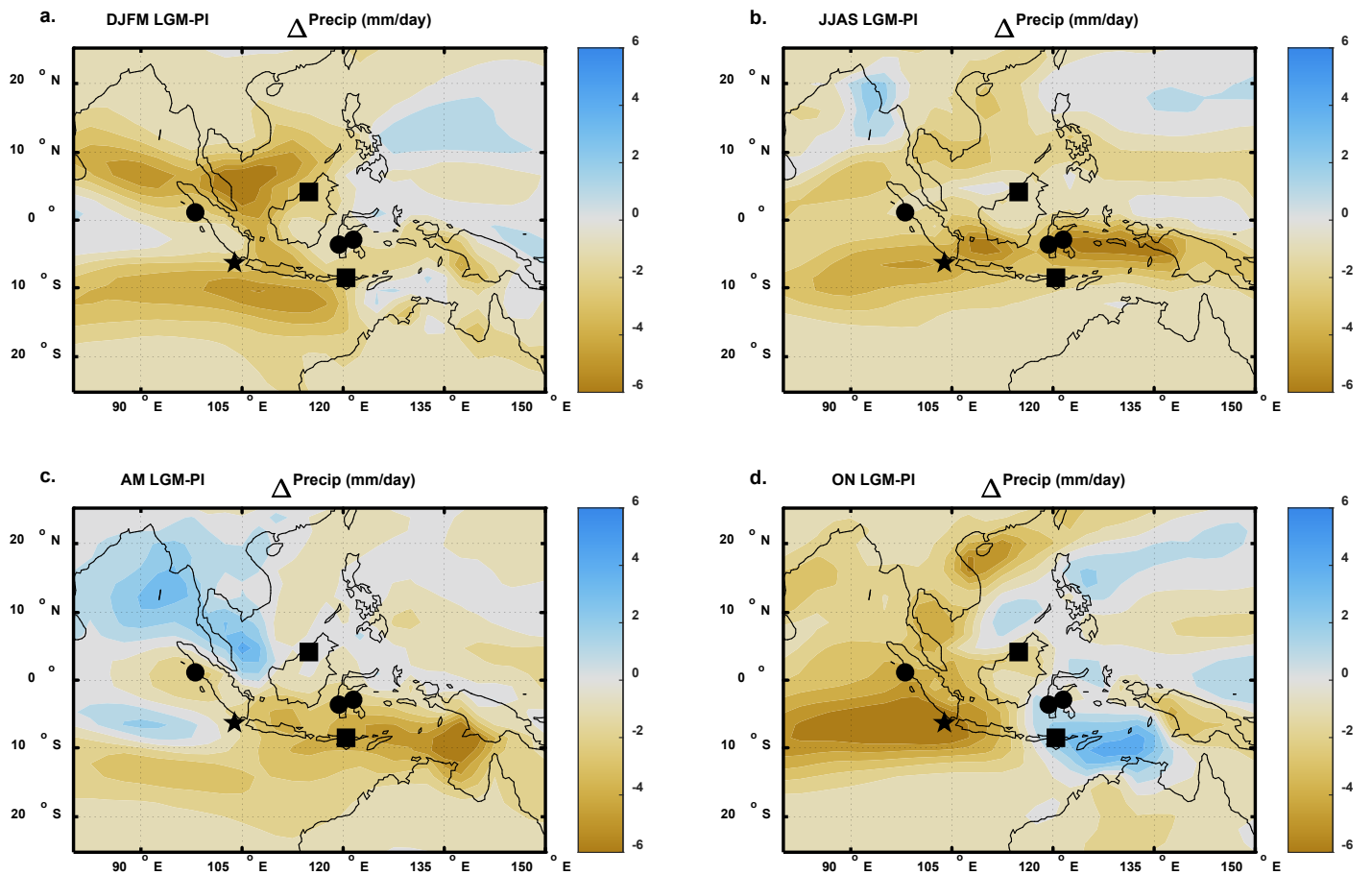


**Figure 7.** As in Figure 6 but depicting the simulated seasonal LGM-PI changes in total precipitation. Shapes indicate location of proxy sites.

Mean annual  $\delta D_{\text{precip}}$  responds differently to LGM GHG (Figure 8a) and ICE (Figure 8b) forcings. The LGM GHG forcing alone results in widespread  $\delta D_{\text{precip}}$  depletion, with enrichment occurring further east over the Pacific Ocean. The LGM ICE forcing results in a spatially distinct pattern of isotopic change similar to the features in the LGM simulation with full forcings (Figure 5b), specifically, depleted  $\delta D_{\text{precip}}$  over the western Pacific and enrichment over the eastern Indian Ocean (Figure 8b).



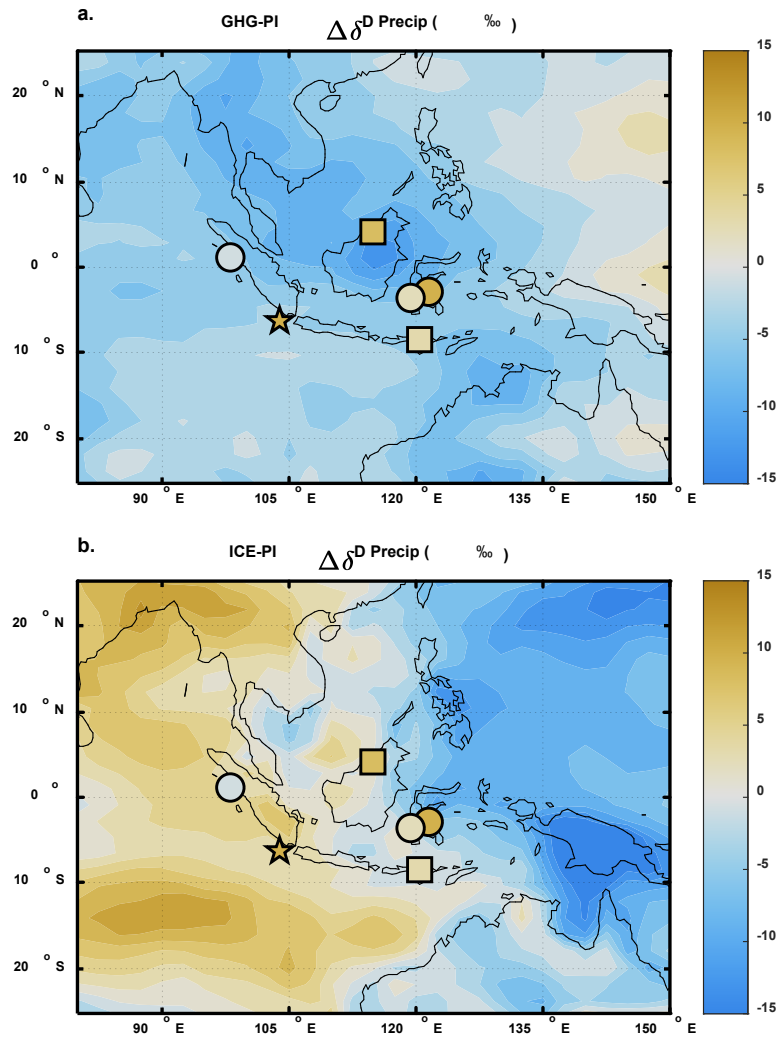


**Figure 8.** Simulated mean annual change in  $\delta D_{\text{precip}}$  from PI control for the a) greenhouse gas and b) ice sheet effects from sensitivity experiments. Filled shapes mark the locations of proxy sites and their calculated LGM-LH isotopic change. All values are reported in VSMOW. Speleothem data are temperature corrected.

#### 4.3 Proxy data-model comparison

The results from our calculations for the magnitude of LGM – LH changes at each location discussed in this text are presented in Table 1. For a direct comparison with the iCESM results, the  $\Delta$ LGM – LH values for each proxy location (Table 1) are presented as the filled shapes in Figures 5b, 6, and 8. In the interest of visualization, we have plotted speleothem changes in  $\delta$ D space by multiplying  $\Delta\delta^{18}\text{O}$  values by eight; however, it should be noted that we have compared them with our simulated LGM-PI  $\Delta\delta^{18}\text{O}_{\text{precip}}$  values and found that our interpretations are unchanged. The LGM-LH differences in paleo-water isotope data from the proxy locations generally agree well with simulated changes except, most notably, Borneo (Figure 5b). Northwest Sumatra is the only proxy site where the LGM is depleted relative to the LH and has the smallest overall change in  $\delta$ D (-0.9‰) reflecting the limited variability in both  $\delta\text{D}_{\text{wax}}$  and  $\delta^{13}\text{C}_{\text{wax}}$  observed in the record (Niedermeyer et al., 2014) and matching the small simulated change in  $\delta\text{D}_{\text{precip}}$  over northern Sumatra, the likely source of the leaf waxes (Figure 5b). Lake Towuti and Mandar Bay record different magnitudes of enrichment, despite their proximity to one another (~7‰ difference), which may be from differences in the spatial integration of leaf waxes at each location or because these sites sit along a strong gradient between enriched and depleted rainfall centers in the model (Figure 5b).

<u>Location</u>	<u>Proxy Type</u>	<u><math>\Delta</math>LGM - LH (‰ VSMOW)</u>	<u>Standard Error (‰ VSMOW)</u>	<u>Temp. Corrected <math>\Delta</math>LGM - LH (‰ VSMOW)</u>
MD98-2152	Leaf Wax $\delta$ D	+9.8	$\pm 1.2$	-
Sumatra	Leaf Wax $\delta$ D	-0.9	$\pm 1.8$	-

Lake Towuti	Leaf Wax $\delta D$	+9.5	$\pm 2.5$	-
Mandar Bay	Leaf Wax $\delta D$	+2.3	$\pm 1.5$	-
Borneo	Speleothem $\delta D$ ( $\delta^{18}O$ )	+15.4 (+1.93)	$\pm 0.2$ ( $\pm 0.03$ )	+8.1 (+1.01)
Flores	Speleothem $\delta D$ ( $\delta^{18}O$ )	+8.3 (+1.04)	$\pm 0.3$ ( $\pm 0.04$ )	+3.1 (+0.39)

**Table 1.** Results for LGM (23 – 19 ka) minus LH (4 – 0 ka) calculations for each proxy location. Proxy type, calculated LGM – LH change, and standard error for the calculation are listed for each location. Note that MD98-2152 results are average glacial-interglacial change (see section 3.4). The temperature corrected LGM – LH changes are listed for the speleothem records and were calculated using Equation 3. The leaf wax changes are  $\delta D$  values. The speleothem changes are listed as  $\delta D$  values, for direct comparison with the leaf wax records, as well as  $\delta^{18}O$  values in parentheses.

To further explore the proxy-model agreement we examine model-proxy scatter plots for the annual average values and the DJFM season, with or without a temperature correction for speleothems (Figure 9). Since the number of data points is small ( $n = 6$ ) we assess the level of agreement by calculating the root mean square error (RMSE) from the 1:1 line (as opposed to fitting a regression). We find that temperature correcting the speleothem data improves the overall agreement. The RMSE between proxy and model mean annual  $\Delta\delta D_{\text{precip}}$  is 10.1‰ with no temperature correction (Figure 9a) and decreases to 8.0‰ after the correction (Figure 9c). From the six proxy locations, two record a sign of LGM-LH change that disagrees with simulated change: Borneo and Sumatra (Figure 9a, 9c), the most northern sites. We further find that proxy  $\delta D_{\text{precip}}$  is unlikely to be uniformly seasonally biased, which is supported by higher RMSEs when seasonal changes in the model are compared with the proxy data. For example, if we assume that proxy  $\delta D_{\text{precip}}$  are biased toward the southern IPWP wet season (DJFM), the

RMSEs increase to 11.9‰ and 10.3‰ for uncorrected and temperature corrected data, respectively (Figure 9b, 9d). Similar results are found when comparing proxy data with simulated  $\delta D_{\text{precip}}$  for JJAS, AM, or ON (Figure S2). It should be noted that Borneo exhibits greater disagreement than the other proxy locations in most cases except JJAS, when it appears to be in the best agreement (Figure S2b). Proxy-model agreement with the LGM ICE experiment (Figure 9e) is greater than the LGM GHG experiment (Figure 9f), suggesting that the LGM ICE forcing exerts the first-order control on  $\delta D_{\text{precip}}$  response.

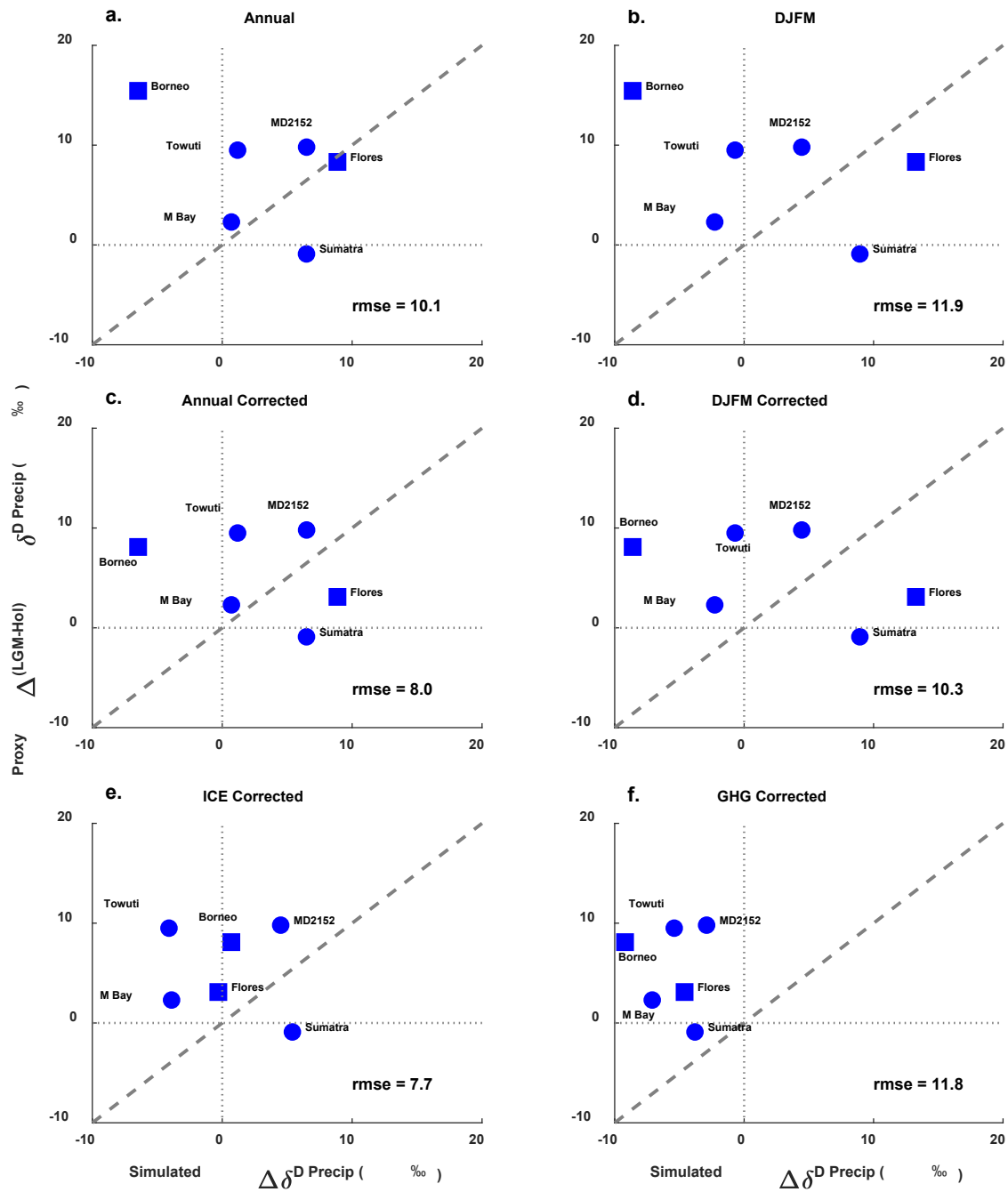


**Figure 9.** Scatterplots of proxy-calculated vs. iCESM simulated  $\delta D_{precip}$  change. Comparison of a) mean annual change at each location with uncorrected speleothem data, b) DJFM change with uncorrected data, c) mean annual change with temperature corrected speleothem data, d) DJFM

change with corrected data, e) ICE simulated change with corrected data, and f) GHG simulated change with corrected data. All data points are labeled by location. Calculated root mean square error (RMSE) is listed in each panel. Dashed gray lines indicate 1:1 line. Dotted crosshairs at point (0,0) are shown in each panel.

## 5 Discussion

### 5.1 Regional mechanisms controlling isotopic change

The similarity of MD98-2152  $\delta D_{\text{precip}}$  between glacial cycles (Figure 4) suggests a consistent glacial – interglacial control on precipitation isotopes over southern Sumatra and western Java. Simulated seasonal changes in precipitation show a greater % change over the southern IPWP during JJAS than in DJFM (see section 4.2), indicating an increase in seasonality of rainfall over this region during glacial climates, specifically, a more intense dry season. Increased rainfall seasonality is supported by previous studies of vegetation changes and geomorphology (Bird et al., 2005; Reeves et al., 2013) as well as several  $\delta^{13}C_{\text{wax}}$  studies, which show increased  $C_4$  vegetation at the LGM, suggesting that glacial increase in the seasonality of rainfall is a common feature across the southern IPWP (Dubois et al., 2014; Russell et al., 2014; Wicaksono et al., 2015, 2017). Additionally, the  $\delta^{13}C_{\text{wax}}$  from MD98-2152 shows that this increase in  $C_4$  vegetation and rainfall seasonality is characteristic of the last five glacial periods and not limited to the LGM (Windler et al., 2019). While simulated changes in rainfall may agree with paleo-evidence of drier, more seasonal conditions during the LGM, the pattern of  $\delta D_{\text{precip}}$  change (Figures 5b and 6) does not strictly follow that of precipitation amount (Figures 5a and 7).

The spatially distinct pattern of simulated mean annual  $\Delta\delta D_{\text{precip}}$  between the Indian Ocean and Pacific Ocean sides of the IPWP (Figure 5b) indicates that water isotopes in the IPWP

are influenced by location-dependent mechanisms. If  $\Delta\delta D_{\text{precip}}$  were linked predominantly to precipitation amount, as classically interpreted, then a widespread decrease in rainfall across the Sunda Shelf and southern IPWP (Figure 5a) would be accompanied by regional enrichment in  $\delta D_{\text{precip}}$ ; however, mean annual  $\delta D_{\text{precip}}$  is depleted in the LGM simulation over the west Pacific, southeast Asia, and Australia for every season (Figures 5b and 6) except JJAS, which shows more of a north-south divide (Figure 6b).

We suggest that the depleted rainfall over the west Pacific (Figures 5b and 6) is a result of regional increases in moisture convergence in the low-to-middle troposphere. Westerly wind anomalies in the LGM simulation between 20°N and the equator (Figure 10) represent the combination of reduced DJFM easterly winds and increased JJAS westerly winds (seasonal wind anomalies are shown in Figure S3). The overall change in the winds highlights the area over the west Pacific (~10°N, 135°E) where winds from the Northern and Southern Hemispheres meet (Figure 10). This anomalous wind pattern is accompanied by stronger upward motion (negative pressure velocity at 850 hPa,  $\omega$ ) over areas near the centers of greatest depletion in  $\delta D_{\text{precip}}$ , namely, the west Pacific at 10°N and Australia at 15°S (Figure 10b vs. 5b). These results indicate increased low-troposphere moisture convergence from distant sources at the LGM that likely drives the depleted isotopic signal over the Pacific side of the IPWP (Figures 5b and 10a). This interpretation is consistent with previous studies showing that precipitation isotope values in large convective systems, such as the IPWP, reflect the isotopic signature of converging water vapor (low  $\delta D$ ) in the atmosphere rather than the surface evaporation signal (high  $\delta D$ ) (Moore et

al., 2014). The  $\delta D$  in converging moisture is lower relative to that at the surface due to the rainout of heavy isotopes along the moisture trajectories (Galewsky et al., 2016; Konecky et al., 2019). Simulated changes in  $\delta D$  of low-level water vapor exhibit centers with depleted values over the west Pacific, supporting this interpretation (Figure 10a).

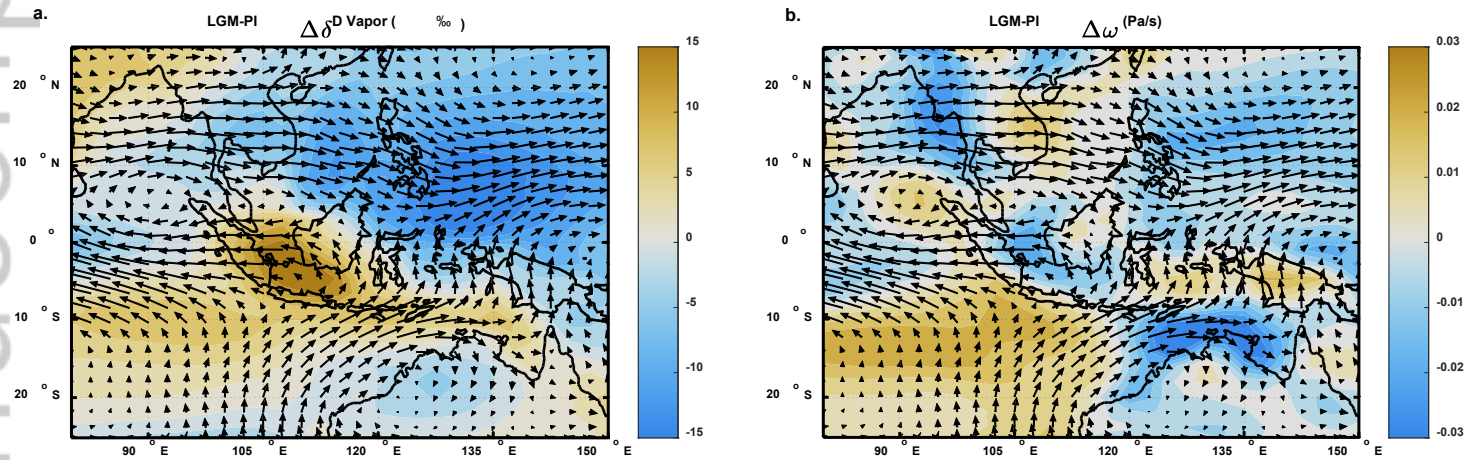


**Figure 10.** Simulated mean annual LGM-PI change in a)  $\delta D$  of water vapor and b) vertical velocity at the 850 hPa level plotted with wind anomalies. Arrows indicate magnitude and direction of anomalies in 850 hPa winds. Proxy locations are excluded from this figure for visual simplicity.

While depleted rainfall over the west Pacific may reflect increased moisture convergence, the simulated enrichment of rainfall over the Indian Ocean and southern IPWP (Figures 5b) likely reflects regional divergence over the tropical eastern Indian Ocean, the Banda Sea, and Papua New Guinea (Figure 10b). Opposite to moisture convergence, the anomalous divergence features more locally derived water vapor, which is isotopically enriched relative to a more distant source. Additionally, anomalous divergence favors rain re-evaporation, one of the microphysical controls on precipitation enrichment where secondary evaporation preferentially



removes lighter isotopes from the condensed raindrops (Dansgaard, 1964). Increased subsidence (more positive  $\omega$ ) across the eastern Indian Ocean (Figure 10b) coincides with the center of greatest  $\delta D_{\text{precip}}$  enrichment in the simulations (Figure 5b). Low-level water vapor becomes enriched over the exposed Sunda Shelf, where ocean did not exist during the LGM, and across the eastern Indian Ocean to the Timor and Arafura Seas (Figure 10a). Additionally, wind vector anomalies show increased easterly wind flow away from the Sumatran coast (Figure 10), suggesting that diverging air, the associated decrease in precipitation, and more locally sourced moisture drive the pattern of isotopic enrichment over the Indian Ocean and southern IPWP.

Previous studies from Mandar Bay (Wicaksono et al., 2017), Lake Towuti (Konecky et al., 2016), and Flores (Ayliffe et al., 2013) have shown either depleted or little-to-no change in precipitation isotope values at the LGM relative to the Holocene, which have been interpreted as an increase in northwest (DJFM) monsoon intensity. These original interpretations were based on proxy data that have been corrected for ice volume effects assuming a spatially homogeneous correction. In contrast to previous studies,  $\delta D_{\text{precip}}$  results shown here have not been corrected for the ice volume effect and the good overall proxy-model agreement tells a different story: during glacial climates, convergence of low-level moisture drove regional isotopic depletion over the western Pacific side of the IPWP, while divergence drove isotopic enrichment across the eastern Indian Ocean and southern IPWP. The enrichment is expressed at MD98-2152, Flores, Lake Towuti, and Mandar Bay. Thus, there is an underlying lesson regarding correcting precipitation isotope proxies using a spatially uniform value for the global ice volume effect. Correcting for

global ice volume is common practice in paleo-water isotope studies; however, it assumes that everywhere on the planet experiences the same net change. While the global deep ocean has been shown to be enriched in  $\delta^{18}\text{O}$  by +1.05‰ during the LGM (Duplessy et al., 2002), surface waters, from which meteoric waters are sourced, can vary widely from that value in different regions. Assuming a 1‰ offset in  $\delta^{18}\text{O}$  prior to interpreting data may obscure the isotopic signature associated with local and regional processes.

The proxy  $\delta D_{\text{precip}}$  change at the two northern sites, Borneo and Sumatra, differ in sign from the simulated  $\delta D_{\text{precip}}$  change (Figures 9a and 9c). Borneo appears to agree best with simulated  $\delta D_{\text{precip}}$  changes during JJAS (Figures 6b and S2), so a seasonal bias in the proxy record could potentially explain this mismatch. Although modern dripwater measurements from Borneo do not suggest that speleothem  $\delta^{18}\text{O}$  are seasonally biased (Cobb et al., 2007) and rainfall amount exhibits little seasonal variability over the northern IPWP (Dubois et al., 2014; Moerman et al., 2013), a potential seasonal bias at the LGM cannot be ruled out. iCESM simulates a larger reduction in precipitation over the Borneo location during DJFM (~20%) relative to JJAS (~8%), indicating an increase in rainfall seasonality over northern Borneo at the LGM (Figure 7; percent change not shown). This result supports the possibility that Borneo speleothems were biased toward JJAS, the relatively wetter season at this location, during the LGM. The change in the Sumatran leaf wax record is quite small (-0.9‰) and the likely source of plant waxes is nearby land (northwest Sumatra) over which LGM-PI  $\delta D_{\text{precip}}$  enrichment is muted (Figure 5b). The change in  $\omega$  and wind vectors (Figure 10) suggest that more moisture may be transported over

the Andaman Sea at the LGM to northwest Sumatra. This remotely sourced moisture would be isotopically depleted, as shown by the depleted  $\delta D$  values of low-level water vapor (Figure 10a), relative to local moisture over northwest Sumatra, potentially resulting in the muted  $\delta D_{\text{precip}}$  enrichment (Figure 5b), a signal that would integrate into the leaf waxes.

Nevertheless, we cannot rule out the possibility that model biases are responsible for the proxy-model disagreement. While iCAM5 simulates observed isotopic variability in tropical convective systems reasonably well (Hu et al., 2018), it is known to have a low convective trigger threshold (Nusbaumer et al., 2017). If the model were overestimating regional convection, then simulated  $\delta D_{\text{precip}}$  could be more depleted than expected in areas with deep convection cells, such as the west Pacific Ocean, likely contributing to the large discrepancy over Borneo (Figure 5b). More modeling studies using multiple state-of-the-art water isotope-enabled models are needed to examine the spatially distinct isotopic responses identified in iCESM.

## 5.2 Climate forcings and the influence of shelf exposure

Proxy data from across the Sunda and Sahul Shelves indicate widespread drying during the LGM (Bird et al., 2005; DiNezio & Tierney, 2013; Reeves et al., 2013) in response to lowered sea level and increased ice sheet albedo (DiNezio et al., 2018). Our sensitivity experiments (Figure 8) similarly indicate that sea level and ice sheet changes are the primary control on precipitation isotopic responses. The LGM ICE simulation produces the same spatial pattern of  $\Delta\delta D_{\text{precip}}$  as the simulation with the full set of forcings (Figure 8b) and generally agrees

with the proxy data (Figure 9e) with centers of depletion over the west Pacific and enrichment over the eastern Indian Ocean.

Exposure of the Sunda and Sahul Shelves during glacial periods increases the distance that air masses pass over land before reaching the IPWP. For instance, moist air masses from the South China Sea would experience more rainout as it travels across the exposed Sunda Shelf, leading to more depleted  $\delta D_{\text{precip}}$  in the central IPWP. Additionally, South China Sea source waters are more depleted in  $\delta D$  relative to the western Pacific and Indian Oceans (Figure 5d; Colin et al., 2010; Waelbroeck et al., 2014). In contrast, simulated  $\Delta \delta D_{\text{precip}}$  over the southwestern IPWP is more enriched at the LGM (Figure 5b), indicating that regional divergence, reduced rainfall, and a more local moisture source (Figure 10b) counteracted the more depleted rainfall from the South China Sea.

Ice sheet albedo and exposure of the Sunda Shelf from lowered sea level at the LGM may have had a particularly large influence on rainfall over Borneo, the site with the largest proxy-model disagreement. Today, rainfall in Borneo is depleted in  $\delta^{18}\text{O}$  during late boreal summer as moisture from the Java Sea gradually rains out along its transport path to northern Borneo (Cobb et al., 2007; Moerman et al., 2013). However, the Java Sea did not exist during glacial periods, so rainfall must have been predominantly from the South China Sea and west Pacific. The LGM ICE simulation shows more enrichment of  $\delta D_{\text{precip}}$  over northwest Borneo than the simulation with all forcings (Figure 8b), suggesting that precipitation isotopes captured by the Borneo speleothems may be more sensitive to changes in ice sheets and sea level than is suggested by

iCESM. Northern Hemisphere ice sheet albedo at the LGM causes dry conditions in southeast Asia and the northern IPWP as cold, dry air overlying the Laurentide ice sheet is advected by mid-latitude westerly winds and mixed equatorward, thus limiting the seasonal advance of boreal monsoons (DiNezio et al., 2018). Borneo could, therefore, primarily be reflecting a remote influence of Northern Hemisphere ice sheet albedo, whereas the more southern proxy locations may reflect the response to the local shelf exposures within the IPWP.

The iCESM simulated change shows a pattern of increased low-level subsidence over the tropical eastern Indian Ocean and anomalous low-level ascension over northern Australia and the western Pacific (Figure 10b), which is consistent with a decoupling of the Indian and Pacific Walker Circulation cells at the LGM, as suggested by recent modeling studies: Walker Circulation weakened over the tropical eastern Indian Ocean (increased subsidence) and accelerated over the western Pacific (increased ascension) (DiNezio et al., 2011, 2016, 2018). A more extensive, cross-sectional view of simulated  $\Delta\omega$  shows that the change in vertical velocity higher in the atmosphere is split over the Maritime Continent (Figure 11a), with centers of anomalous subsidence over the Indian Ocean side and anomalous ascension over the Pacific side. Stronger  $\omega$  in the western Indian Ocean near East Africa accompanies the increased subsidence in the eastern Indian Ocean and the stronger  $\omega$  over the west Pacific is paired with anomalous subsidence in the eastern Pacific near South America (Figure 11a), emphasizing the different Walker responses between the basins. Likewise, the different  $\Delta\omega$  in our GHG (Figure 11b) and ICE (Figure 11c) simulations highlights that the patterns of change between the different basins

are influenced by different climate forcings, specifically, ice sheet albedo and the associated lowering of sea level over the Indian Ocean and GHG concentrations over the Pacific. Closer examination of  $\Delta\omega$  over the Maritime Continent shows that the dual centers of increased ascension over the western Pacific in the full forcing simulation likely result from a combination of GHG and ICE forcings (Figure 11). Overall, reduced sea level and ice sheet albedo are primary drivers of the proxy-measured spatial pattern of the hydroclimate response to glacial conditions in the IPWP, including the dynamics governing precipitation isotopes.

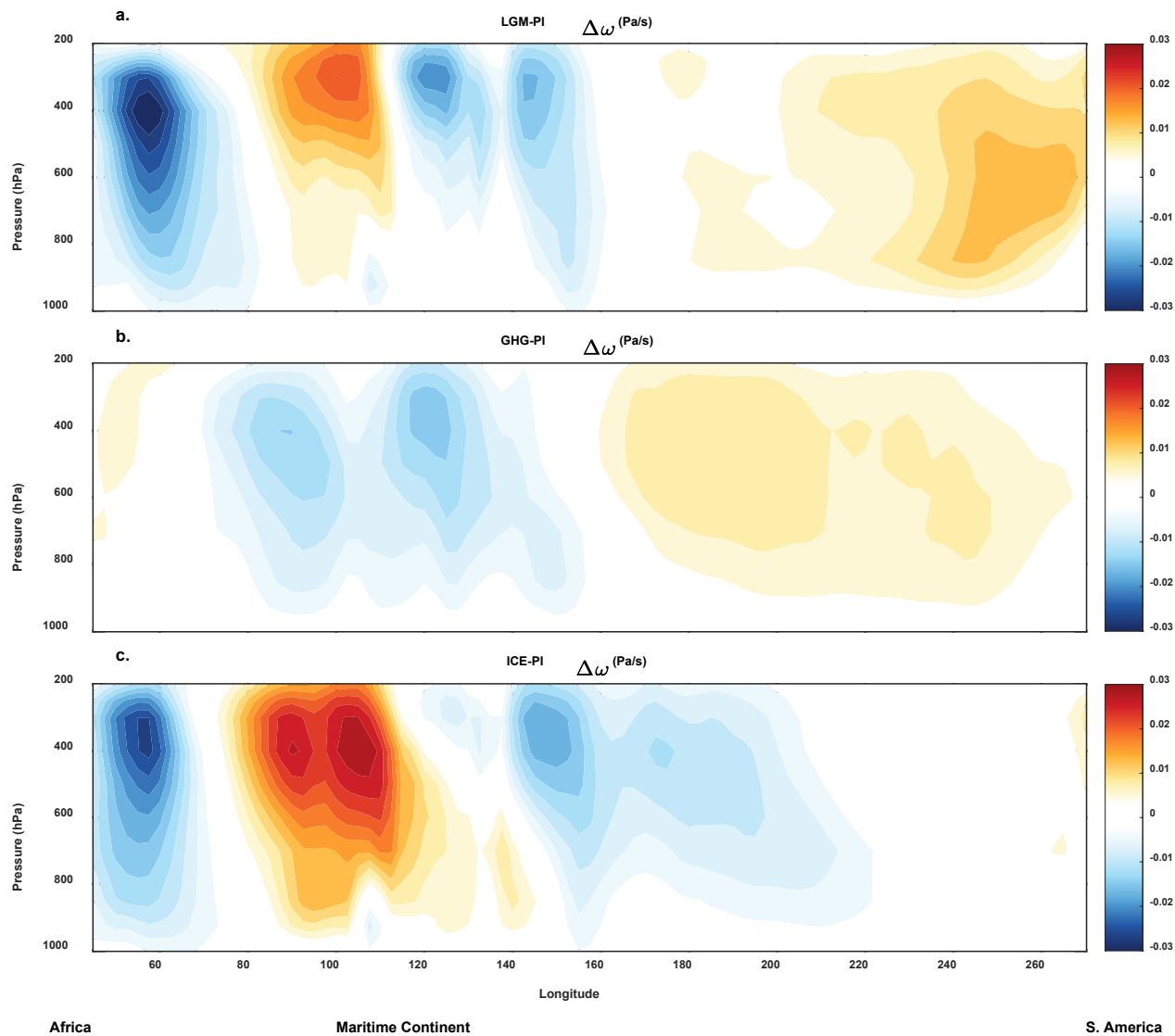


**Figure 11.** Simulated tropical mean annual  $\Delta\omega$  at different atmospheric pressure levels averaged over 10°N to 10°S for a) the LGM-PI (full forcing), b) GHG-PI, and c) ICE-PI simulations. Data plotted spans longitudinally from the western Indian to the eastern Pacific Oceans. Reference landmarks are indicated at the bottom.

## 6 Conclusions

Our new  $\delta D_{\text{precip}}$  record from MD98-2152 suggests consistent glacial enrichment of precipitation isotopes over southern Sumatra and western Java for the last 450 kyr. Isotope-enabled simulations using iCESM display a good match between proxy and model change in  $\delta D_{\text{precip}}$  during the LGM and shed light on mechanisms controlling regional precipitation isotopes over the IPWP during glacial periods. The distinctive spatial pattern of simulated  $\delta D_{\text{precip}}$  change—depleted rainfall over the west Pacific and enriched rainfall over the eastern Indian Ocean and southern IPWP—does not strictly follow the pattern of reduced precipitation across the IPWP, suggesting that different mechanisms controlled the isotopic value of rainfall in each area during glacial times. Regional increases in low-level moisture convergence contributed to depletion of  $\delta D_{\text{precip}}$  in the west Pacific, whereas increased subsidence, the reduction of rainfall, and more localized moisture sources drove enrichment over the eastern Indian Ocean and southern IPWP.

Overall, this study presents a new picture of the mechanisms controlling precipitation isotope variability in the IPWP during glacial climates. Previously, proxy data from Mandar Bay, Lake Towuti, and Flores were interpreted to indicate an intensified northwest monsoon during glacial periods; in contrast, our study suggests that these locations experienced glacial enrichment due to increases in regional low-level subsidence. We have shown that the primary mechanisms controlling precipitation isotopes in the IPWP during glacial periods are ice sheet forcing and the associated lowering in sea level, but not the lower greenhouse gases. The decoupling of the Indian and Pacific Walker Circulation cells at the LGM likely resulted in



different regional circulation changes between the two basins, which contributed to the distinct spatial pattern of  $\Delta\delta D_{\text{precip}}$ . Lastly, we caution against applying a uniform ice volume-correction to precipitation isotope records prior to interpretation, as it may mask local processes when comparing different locations.

## Acknowledgments

Funding for this study was provided by the David and Lucile Packard Foundation Fellowship in Science and Engineering to J.E. Tierney, by the National Science Foundation Graduate Research Fellowship Program to G. Windler (grant no. DGE-1746060), and by the Heising-Simons Foundation to J.E. Tierney and C.J. Poulsen (grant no. 2016-015). We thank P. Murphy for technical support and J.B. Wurtzel for guidance using HYSPLIT4. The MD98-2152  $\delta D$  data generated in this study are available from NOAA's National Centers for Environmental Information Paleoclimate page: <https://www.ncdc.noaa.gov/paleo/study/30533>. Model data is available through Tierney et al. (2020). Other data used in this study are available as follows: Borneo speleothems through Partin et al. (2007), northwest Sumatra leaf waxes through Niedermeyer et al. (2014), Mandar Bay leaf waxes through Wicaksono et al. (2017), Lake Towuti  $\delta D_{\text{wax}}$  through Konecky et al. (2016) and  $\delta^{13}C_{\text{wax}}$  through Russell et al. (2014), Flores speleothems through Ayliffe et al. (2013), MD98-2152  $\delta^{13}C_{\text{wax}}$  through Windler et al. (2019), and the iCESM Last Millennium Ensemble through Brady et al. (2019).

## References

Aggarwal, P. K., Alduchov, O. A., Froehlich, K. O., Araguas-Araguas, L. J., Sturchio, N. C., &

- Kurita, N. (2012). Stable isotopes in global precipitation: A unified interpretation based on atmospheric moisture residence time. *Geophysical Research Letters*, 39(11), L11705. <https://doi.org/10.1029/2012GL051937>
- Aggarwal, P. K., Romatschke, U., Araguas-Araguas, L., Belachew, D., Longstaffe, F. J., Berg, P., et al. (2016). Proportions of convective and stratiform precipitation revealed in water isotope ratios. *Nature Geoscience*, 9(8), 624–629. <https://doi.org/10.1038/ngeo2739>
- Aldrian, E., & Susanto, R. D. (2003). Identification of three dominant rainfall regions within Indonesia and their relationship to sea surface temperature. *International Journal of Climatology*, 23(12), 1435–1452. <https://doi.org/10.1002/joc.950>
- Ayliffe, L. K., Gagan, M. K., Zhao, J., Drysdale, R. N., Hellstrom, J. C., Hantoro, W. S., et al. (2013). Rapid interhemispheric climate links via the Australasian monsoon during the last deglaciation. *Nature Communications*, 4(1), 2908. <https://doi.org/10.1038/ncomms3908>
- Belgaman, H. A., Ichiyanagi, K., Suwarman, R., Tanoue, M., Aldrian, E., Utami, A. I. D., & Kusumaningtyas, S. D. A. (2017). Characteristics of seasonal precipitation isotope variability in Indonesia. *Hydrological Research Letters*, 11(2), 92–98. <https://doi.org/10.3178/hrl.11.92>
- Bhattacharya, T., Tierney, J. E., Addison, J. A., & Murray, J. W. (2018). Ice-sheet modulation of deglacial North American monsoon intensification. *Nature Geoscience*, 11(11), 848–852. <https://doi.org/10.1038/s41561-018-0220-7>
- Bird, M. I., Taylor, D., & Hunt, C. (2005). Palaeoenvironments of insular Southeast Asia during

the Last Glacial Period: a savanna corridor in Sundaland? *Quaternary Science Reviews*, 24(20–21), 2228–2242. <https://doi.org/10.1016/j.quascirev.2005.04.004>

Brady, E., Stevenson, S., Bailey, D., Liu, Z., Noone, D., Nusbaumer, J., et al. (2019). The Connected Isotopic Water Cycle in the Community Earth System Model Version 1. *Journal of Advances in Modeling Earth Systems*, 11(8), 2547–2566.

<https://doi.org/10.1029/2019MS001663>

Bronk Ramsey, C. (2008). Deposition models for chronological records. *Quaternary Science Reviews*, 27(1–2), 42–60. <https://doi.org/10.1016/j.quascirev.2007.01.019>

Clark, I., & Fritz, P. (1997). *Environmental Isotopes in Hydrogeology*. CRC Press.

Cobb, K. M., Adkins, J. F., Partin, J. W., & Clark, B. (2007). Regional-scale climate influences on temporal variations of rainwater and cave dripwater oxygen isotopes in northern Borneo. *Earth and Planetary Science Letters*, 263(3–4), 207–220.

<https://doi.org/10.1016/j.epsl.2007.08.024>

Colin, C., Siani, G., Sicre, M.-A., & Liu, Z. (2010). Impact of the East Asian monsoon rainfall changes on the erosion of the Mekong River basin over the past 25,000yr. *Marine Geology*, 271(1–2), 84–92. <https://doi.org/10.1016/j.margeo.2010.01.013>

Coplen, T. B., Kendall, C., & Hopple, J. (1983). Comparison of isotope reference samples. *Nature*, 302(21), 236–238.

Dansgaard, W. (1964). Stable isotopes in precipitation. *Tellus*, 16(4), 436–468.

<https://doi.org/10.3402/tellusa.v16i4.8993>

- DiNezio, P. N., Clement, A., Vecchi, G. A., Soden, B., Broccoli, A. J., Otto-Bliesner, B. L., & Braconnot, P. (2011). The response of the Walker circulation to Last Glacial Maximum forcing: Implications for detection in proxies. *Paleoceanography*, 26(3), n/a-n/a. <https://doi.org/10.1029/2010PA002083>
- DiNezio, Pedro N., & Tierney, J. E. (2013). The effect of sea level on glacial Indo-Pacific climate. *Nature Geoscience*, 6(6), 485–491. <https://doi.org/10.1038/ngeo1823>
- DiNezio, Pedro N., Timmermann, A., Tierney, J. E., Jin, F.-F., Otto-Bliesner, B., Rosenbloom, N., et al. (2016). The climate response of the Indo-Pacific warm pool to glacial sea level. *Paleoceanography*, 31(6), 866–894. <https://doi.org/10.1002/2015PA002890>
- DiNezio, Pedro N., Tierney, J. E., Otto-Bliesner, B. L., Timmermann, A., Bhattacharya, T., Rosenbloom, N., & Brady, E. (2018). Glacial changes in tropical climate amplified by the Indian Ocean. *Science Advances*, 4(12), eaat9658. <https://doi.org/10.1126/sciadv.aat9658>
- Draxler, R. R. (1999). HYSPLIT4 user's guide. *NOAA Technical Memorandum ERL ARL-230*.
- Dubois, N., Oppo, D. W., Galy, V. V., Mohtadi, M., van der Kaars, S., Tierney, J. E., et al. (2014). Indonesian vegetation response to changes in rainfall seasonality over the past 25,000 years. *Nature Geoscience*, 7(7), 513–517. <https://doi.org/10.1038/ngeo2182>
- Duplessy, J.-C., Labeyrie, L., & Waelbroeck, C. (2002). Constraints on the ocean oxygen isotopic enrichment between the Last Glacial Maximum and the Holocene: Paleoceanographic implications. *Quaternary Science Reviews*, 21(1–3), 315–330. [https://doi.org/10.1016/S0277-3791\(01\)00107-X](https://doi.org/10.1016/S0277-3791(01)00107-X)

- Eglinton, G., & Hamilton, R. J. (1967). Leaf Epicuticular Waxes. *Science*, 156(3780), 1322–1335. <https://doi.org/10.1126/science.156.3780.1322>
- Eglinton, T. I., & Eglinton, G. (2008). Molecular proxies for paleoclimatology. *Earth and Planetary Science Letters*, 275(1–2), 1–16. <https://doi.org/10.1016/j.epsl.2008.07.012>
- Feakins, S. J., Eglinton, T. I., & DeMenocal, P. B. (2007). A comparison of biomarker records of northeast African vegetation from lacustrine and marine sediments (ca. 3.40Ma). *Organic Geochemistry*, 38(10), 1607–1624. <https://doi.org/10.1016/j.orggeochem.2007.06.008>
- Galewsky, J., Steen-Larsen, H. C., Field, R. D., Worden, J., Risi, C., & Schneider, M. (2016). Stable isotopes in atmospheric water vapor and applications to the hydrologic cycle. *Reviews of Geophysics*, 54(4), 809–865. <https://doi.org/10.1002/2015RG000512>
- Gao, L., Edwards, E. J., Zeng, Y., & Huang, Y. (2014). Major Evolutionary Trends in Hydrogen Isotope Fractionation of Vascular Plant Leaf Waxes. *PLoS ONE*, 9(11), e112610. <https://doi.org/10.1371/journal.pone.0112610>
- Garcin, Y., Schefuß, E., Schwab, V. F., Garreta, V., Gleixner, G., Vincens, A., et al. (2014). Reconstructing C3 and C4 vegetation cover using n-alkane carbon isotope ratios in recent lake sediments from Cameroon, Western Central Africa. *Geochimica et Cosmochimica Acta*, 142, 482–500. <https://doi.org/10.1016/j.gca.2014.07.004>
- Griffiths, M. L., Drysdale, R. N., Gagan, M. K., Zhao, J. -x., Ayliffe, L. K., Hellstrom, J. C., et al. (2009). Increasing Australian–Indonesian monsoon rainfall linked to early Holocene sea-level rise. *Nature Geoscience*, 2(9), 636–639. <https://doi.org/10.1038/ngeo605>

Heaney, L. R. (1991). A synopsis of climatic and vegetational change in Southeast Asia.

*Climatic Change*, 19(1–2), 53–61. <https://doi.org/10.1007/BF00142213>

Hu, J., Emile-Geay, J., Nusbaumer, J., & Noone, D. (2018). Impact of Convective Activity on

Precipitation  $\delta^{18}\text{O}$  in Isotope-Enabled General Circulation Models. *Journal of Geophysical Research: Atmospheres*, 123(23). <https://doi.org/10.1029/2018JD029187>

IAEA/WMO. (2019). Global Network of Isotopes in Precipitation.

Jasechko, S., Lechler, A., Pausata, F. S. R., Fawcett, P. J., Gleeson, T., Cendón, D. I., et al.

(2015). Late-glacial to late-Holocene shifts in global precipitation  $\delta^{18}\text{O}$ . *Climate of the Past*, 11(10), 1375–1393. <https://doi.org/10.5194/cp-11-1375-2015>

Kageyama, M., Albani, S., Braconnot, P., Harrison, S. P., Hopcroft, P. O., Ivanovic, R. F., et al.

(2017). The PMIP4 contribution to CMIP6 – Part 4: Scientific objectives and experimental design of the PMIP4-CMIP6 Last Glacial Maximum experiments and PMIP4 sensitivity experiments. *Geoscientific Model Development*, 10(11), 4035–4055.

<https://doi.org/10.5194/gmd-10-4035-2017>

Kim, S.-T., & O’Neil, J. R. (1997). Equilibrium and nonequilibrium oxygen isotope effects in synthetic carbonates. *Geochimica et Cosmochimica Acta*, 61(16), 3461–3475.

Konecky, B., Russell, J., & Bijaksana, S. (2016). Glacial aridity in central Indonesia coeval with

intensified monsoon circulation. *Earth and Planetary Science Letters*, 437, 15–24. <https://doi.org/10.1016/j.epsl.2015.12.037>

Konecky, B. L., Noone, D. C., & Cobb, K. M. (2019). The Influence of Competing

Hydroclimate Processes on Stable Isotope Ratios in Tropical Rainfall. *Geophysical Research Letters*, 46(3), 1622–1633. <https://doi.org/10.1029/2018GL080188>

Kurita, N. (2013). Water isotopic variability in response to mesoscale convective system over the tropical ocean. *Journal of Geophysical Research: Atmospheres*, 118(18), 10,376–10,390. <https://doi.org/10.1002/jgrd.50754>

Kurita, N., Ichiyanagi, K., Matsumoto, J., Yamanaka, M. D., & Ohata, T. (2009). The relationship between the isotopic content of precipitation and the precipitation amount in tropical regions. *Journal of Geochemical Exploration*, 102(3), 113–122. <https://doi.org/10.1016/j.gexplo.2009.03.002>

Kusch, S., Rethemeyer, J., Schefuß, E., & Mollenhauer, G. (2010). Controls on the age of vascular plant biomarkers in Black Sea sediments. *Geochimica et Cosmochimica Acta*, 74(24), 7031–7047. <https://doi.org/10.1016/j.gca.2010.09.005>

Lisiecki, L. E., & Raymo, M. E. (2005). A Pliocene-Pleistocene stack of 57 globally distributed benthic  $\delta^{18}\text{O}$  records. *Paleoceanography*, 20(1), PA 1003. <https://doi.org/10.1029/2004PA001071>

Menne, M. J., Durre, I., Vose, R. S., Gleason, B. E., & Houston, T. G. (2012). An Overview of the Global Historical Climatology Network-Daily Database. *Journal of Atmospheric and Oceanic Technology*, 29(7), 897–910. <https://doi.org/10.1175/JTECH-D-11-00103.1>

Moerman, J. W., Cobb, K. M., Adkins, J. F., Sodemann, H., Clark, B., & Tuen, A. A. (2013). Diurnal to interannual rainfall  $\delta^{18}\text{O}$  variations in northern Borneo driven by regional

hydrology. *Earth and Planetary Science Letters*, 369–370, 108–119.

<https://doi.org/10.1016/j.epsl.2013.03.014>

Moore, M., Kuang, Z., & Blossey, P. N. (2014). A moisture budget perspective of the amount effect. *Geophysical Research Letters*, 41(4), 1329–1335.

<https://doi.org/10.1002/2013GL058302>

Niedermeyer, E. M., Sessions, A. L., Feakins, S. J., & Mohtadi, M. (2014). Hydroclimate of the western Indo-Pacific Warm Pool during the past 24,000 years. *Proceedings of the National Academy of Sciences*, 111(26), 9402–9406. <https://doi.org/10.1073/pnas.1323585111>

Nusbaumer, J., Wong, T. E., Bardeen, C., & Noone, D. (2017). Evaluating hydrological processes in the Community Atmosphere Model Version 5 (CAM5) using stable isotope ratios of water. *Journal of Advances in Modeling Earth Systems*, 9(2), 949–977.

<https://doi.org/10.1002/2016MS000839>

Partin, J. W., Cobb, K. M., Adkins, J. F., Clark, B., & Fernandez, D. P. (2007). Millennial-scale trends in west Pacific warm pool hydrology since the Last Glacial Maximum. *Nature*, 449(7161), 452–455. <https://doi.org/10.1038/nature06164>

Reeves, J. M., Bostock, H. C., Ayliffe, L. K., Barrows, T. T., De Deckker, P., Devriendt, L. S., et al. (2013). Palaeoenvironmental change in tropical Australasia over the last 30,000 years – a synthesis by the OZ-INTIMATE group. *Quaternary Science Reviews*, 74, 97–114.

<https://doi.org/10.1016/j.quascirev.2012.11.027>

Rozanski, K., Araguas-Araguas, L., & Gonfiantini, R. (1993). Isotopic Patterns in Modern



Global Precipitation. In *Climate Change in Continental Isotope Records*. American Geophysical Union Monograph.

Russell, J. M., Vogel, H., Konecky, B. L., Bijaksana, S., Huang, Y., Melles, M., et al. (2014).

Glacial forcing of central Indonesian hydroclimate since 60,000 y B.P. *Proceedings of the National Academy of Sciences*, 111(14), 5100–5105.

<https://doi.org/10.1073/pnas.1402373111>

Sachse, D., Billault, I., Bowen, G. J., Chikaraishi, Y., Dawson, T. E., Feakins, S. J., et al. (2012).

Molecular Paleohydrology: Interpreting the Hydrogen-Isotopic Composition of Lipid Biomarkers from Photosynthesizing Organisms. *Annual Review of Earth and Planetary Sciences*, 40(1), 221–249. <https://doi.org/10.1146/annurev-earth-042711-105535>

Schott, F. A., & McCreary, J. P. (2001). The monsoon circulation of the Indian Ocean. *Progress in Oceanography*, 51(1), 1–123. [https://doi.org/10.1016/S0079-6611\(01\)00083-0](https://doi.org/10.1016/S0079-6611(01)00083-0)

Stevenson, S., Otto-Bliesner, B. L., Brady, E. C., Nusbaumer, J., Tabor, C., Tomas, R., et al.

(2019). Volcanic Eruption Signatures in the Isotope-Enabled Last Millennium Ensemble. *Paleoceanography and Paleoclimatology*, 34(8), 1534–1552.

<https://doi.org/10.1029/2019PA003625>

Thirumalai, K., DiNezio, P. N., Tierney, J. E., Puy, M., & Mohtadi, M. (2019). An El Niño

Mode in the Glacial Indian Ocean? *Paleoceanography and Paleoclimatology*, 34(8), 1316–1327. <https://doi.org/10.1029/2019PA003669>

Tierney, J., Pausata, F. S. R., & DeMenocal, P. B. (2017). Rainfall regimes of the Green Sahara.

*Science Advances*, 3(1), e1601503. <https://doi.org/10.1126/sciadv.1601503>

Tierney, J. E., Oppo, D. W., Rosenthal, Y., Russell, J. M., & Linsley, B. K. (2010). Coordinated hydrological regimes in the Indo-Pacific region during the past two millennia.

*Paleoceanography*, 25(1), 1–7. <https://doi.org/10.1029/2009PA001871>

Tierney, J. E., Oppo, D. W., Legrande, A. N., Huang, Y., Rosenthal, Y., & Linsley, B. K. (2012).

The influence of Indian Ocean atmospheric circulation on Warm Pool hydroclimate during the Holocene epoch. *Journal of Geophysical Research Atmospheres*, 117(19), 1–9.

<https://doi.org/10.1029/2012JD018060>

Tierney, Jessica E, Zhu, J., King, J., Malevich, S. B., Hakim, G. J., & Poulsen, C. J. (2020).

Glacial cooling and climate sensitivity revisited. *Nature*, 584(7822), 569–573.

<https://doi.org/10.1038/s41586-020-2617-x>

Volkman, J. K., Johns, R. B., Gillan, F. T., Perry, G. J., & Bavor, H. J. (1980). Microbial lipids

of an intertidal sediment—I. Fatty acids and hydrocarbons. *Geochimica et Cosmochimica Acta*, 44(8), 1133–1143. [https://doi.org/10.1016/0016-7037\(80\)90067-8](https://doi.org/10.1016/0016-7037(80)90067-8)

Waelbroeck, C., Kiefer, T., Dokken, T., Chen, M.-T., Spero, H. J., Jung, S., et al. (2014).

Constraints on surface seawater oxygen isotope change between the Last Glacial Maximum and the Late Holocene. *Quaternary Science Reviews*, 105, 102–111.

<https://doi.org/10.1016/j.quascirev.2014.09.020>

Wicaksono, S. A., Russell, J. M., & Bijaksana, S. (2015). Compound-specific carbon isotope

records of vegetation and hydrologic change in central Sulawesi, Indonesia, since 53,000 yr

BP. *Palaeogeography, Palaeoclimatology, Palaeoecology*, 430, 47–56.

<https://doi.org/10.1016/j.palaeo.2015.04.016>

Wicaksono, S. A., Russell, J. M., Holbourn, A., & Kuhnt, W. (2017). Hydrological and vegetation shifts in the Wallacean region of central Indonesia since the Last Glacial Maximum. *Quaternary Science Reviews*, 157, 152–163.

<https://doi.org/10.1016/j.quascirev.2016.12.006>

Windler, G., Tierney, J. E., DiNezio, P. N., Gibson, K., & Thunell, R. (2019). Shelf exposure influence on Indo-Pacific Warm Pool climate for the last 450,000 years. *Earth and Planetary Science Letters*, 516, 66–76. <https://doi.org/10.1016/j.epsl.2019.03.038>

Wong, T. E., Nusbaumer, J., & Noone, D. C. (2017). Evaluation of modeled land-atmosphere exchanges with a comprehensive water isotope fractionation scheme in version 4 of the Community Land Model. *Journal of Advances in Modeling Earth Systems*, 9(2), 978–1001.

<https://doi.org/10.1002/2016MS000842>

Wu, P., Hara, M., Hamada, J., Yamanaka, M. D., & Kimura, F. (2009). Why a Large Amount of Rain Falls over the Sea in the Vicinity of Western Sumatra Island during Nighttime. *Journal of Applied Meteorology and Climatology*, 48(7), 1345–1361.

<https://doi.org/10.1175/2009JAMC2052.1>

Wurtzel, J. B., Abram, N. J., Lewis, S. C., Bajo, P., Hellstrom, J. C., Troitzsch, U., & Heslop, D. (2018). Tropical Indo-Pacific hydroclimate response to North Atlantic forcing during the last deglaciation as recorded by a speleothem from Sumatra, Indonesia. *Earth and Planetary*

*Science Letters*, 492, 264–278. <https://doi.org/10.1016/j.epsl.2018.04.001>

Zhang, J., Liu, Z., Brady, E. C., Oppo, D. W., Clark, P. U., Jahn, A., et al. (2017). Asynchronous warming and  $\delta^{18}\text{O}$  evolution of deep Atlantic water masses during the last deglaciation.

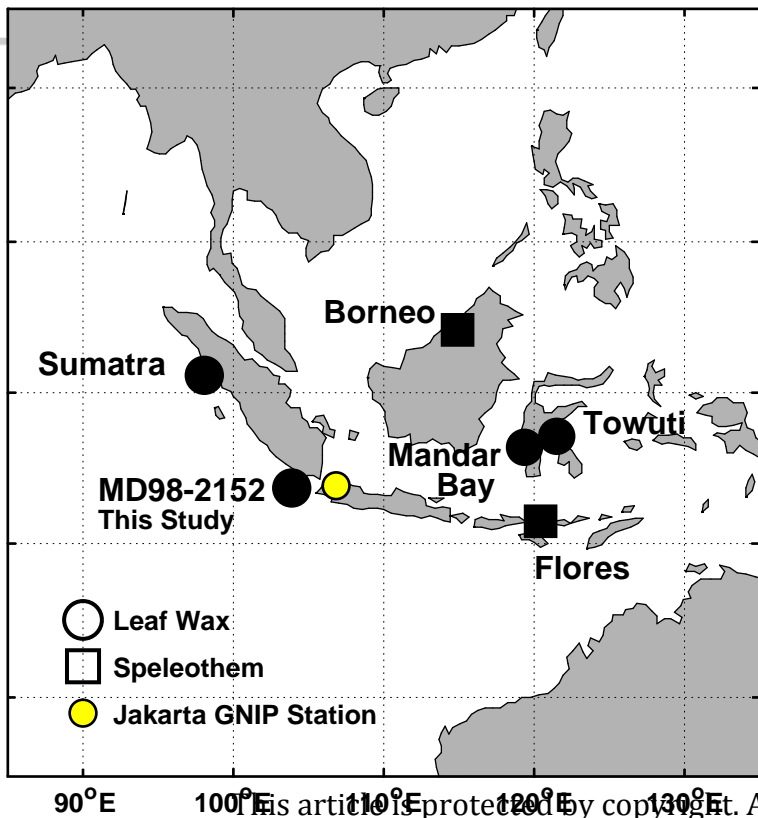
*Proceedings of the National Academy of Sciences*, 114(42), 11075–11080.

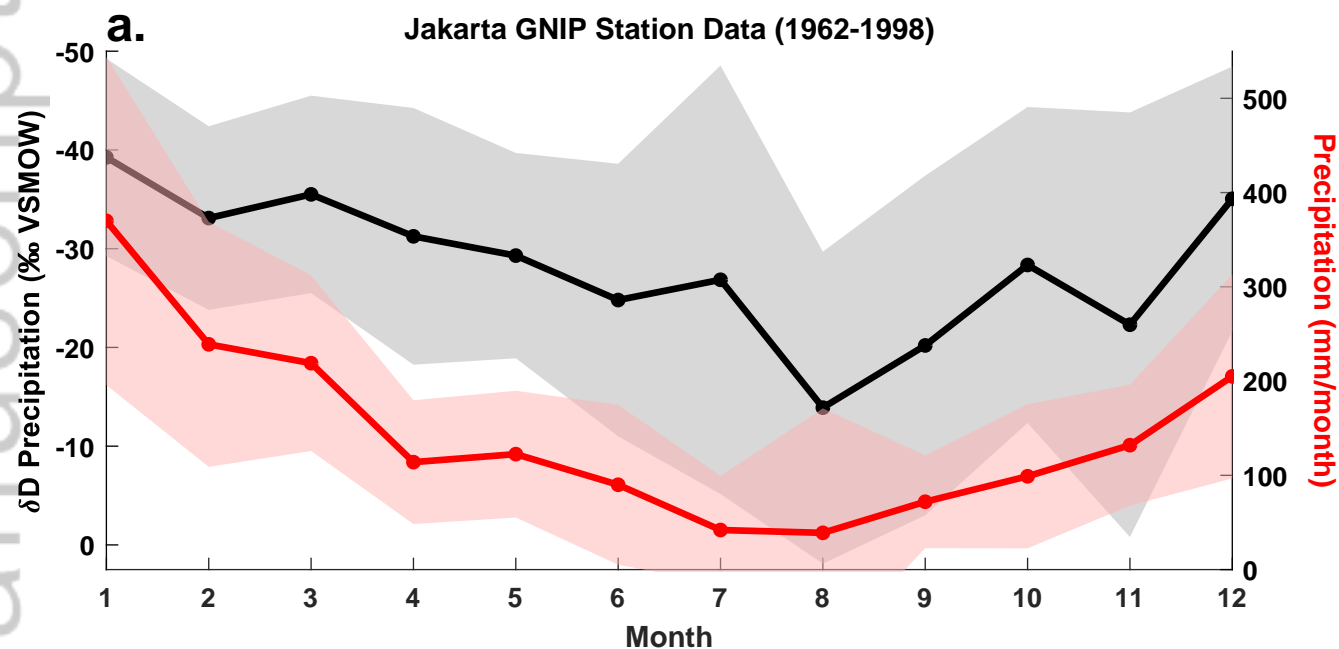
<https://doi.org/10.1073/pnas.1704512114>

Zhu, J., Liu, Z., Brady, E., Otto-Bliesner, B., Zhang, J., Noone, D., et al. (2017). Reduced ENSO variability at the LGM revealed by an isotope-enabled Earth system model. *Geophysical*

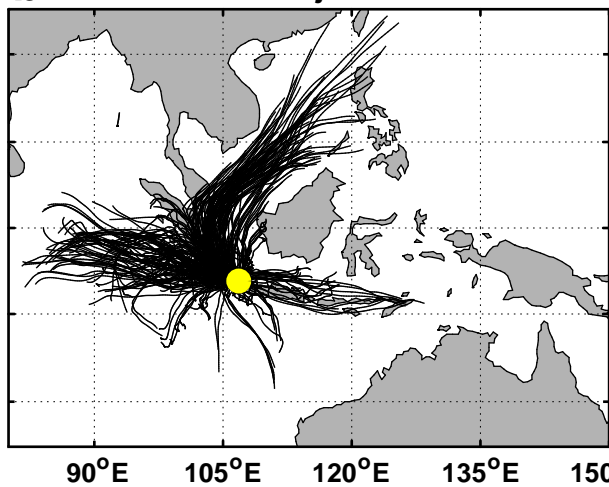
*Research Letters*, 44(13), 6984–6992. <https://doi.org/10.1002/2017GL073406>

Author Manuscript

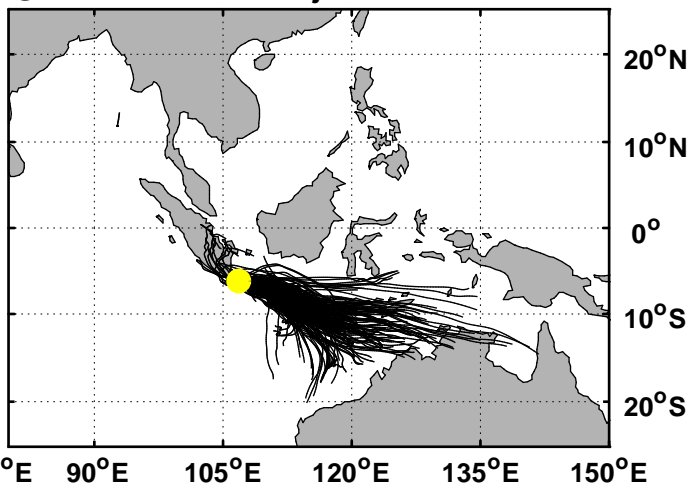




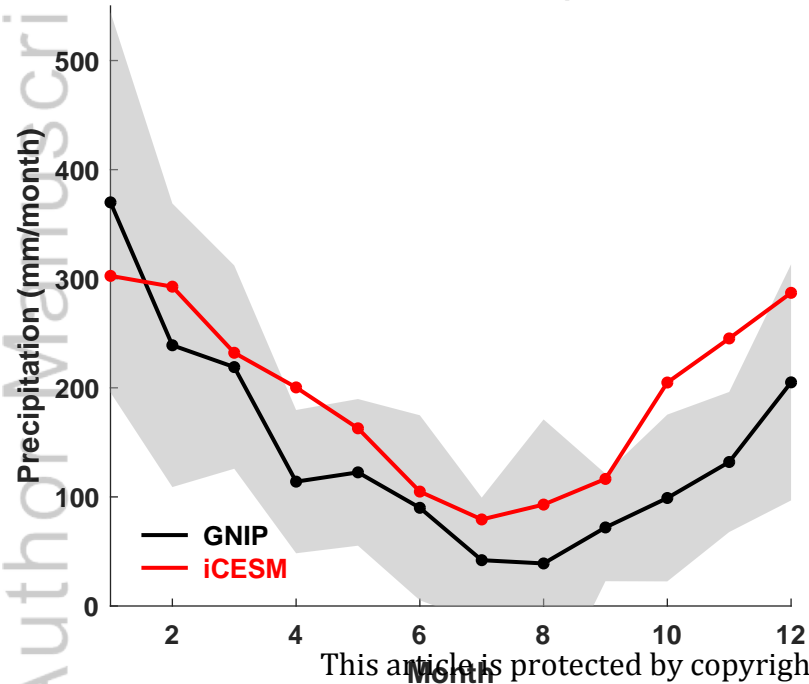
**b.** DJFM Trajectories



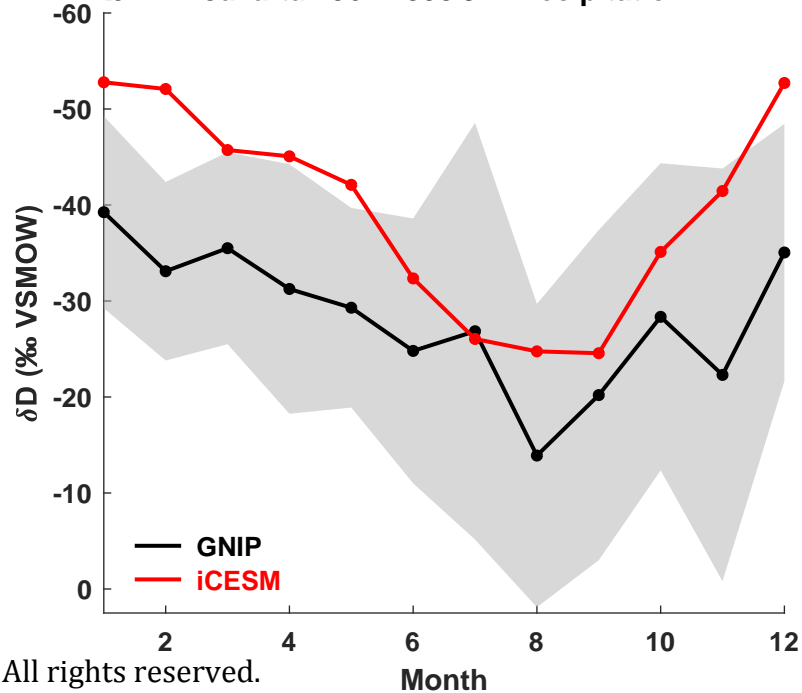
**c.** JJAS Trajectories



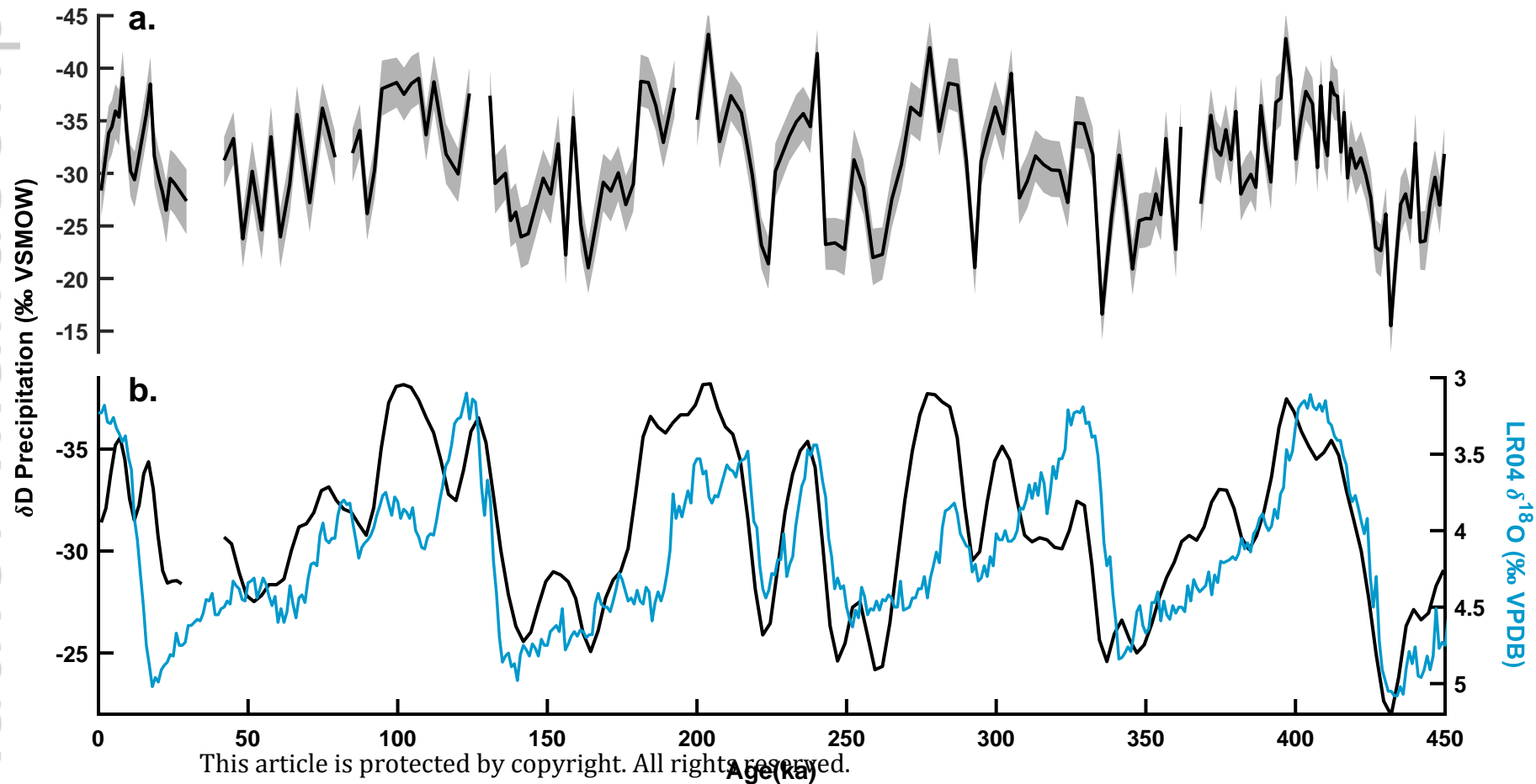
**a.** Jakarta 1962-1998 Precipitation



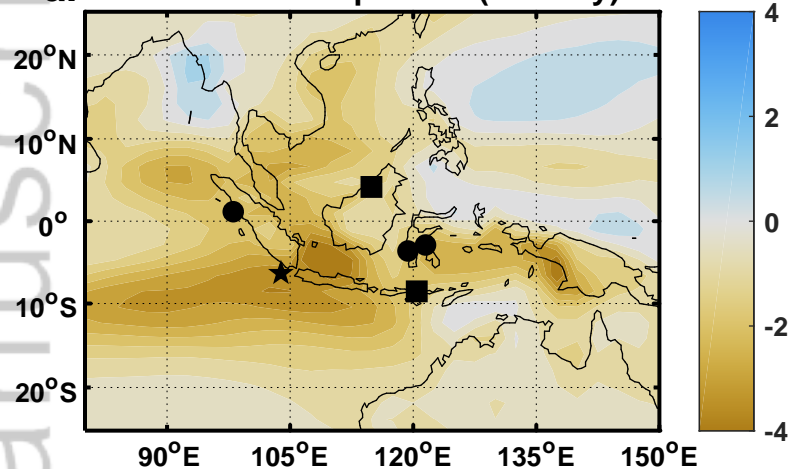
**b.** Jakarta 1962-1998  $\delta D$  Precipitation



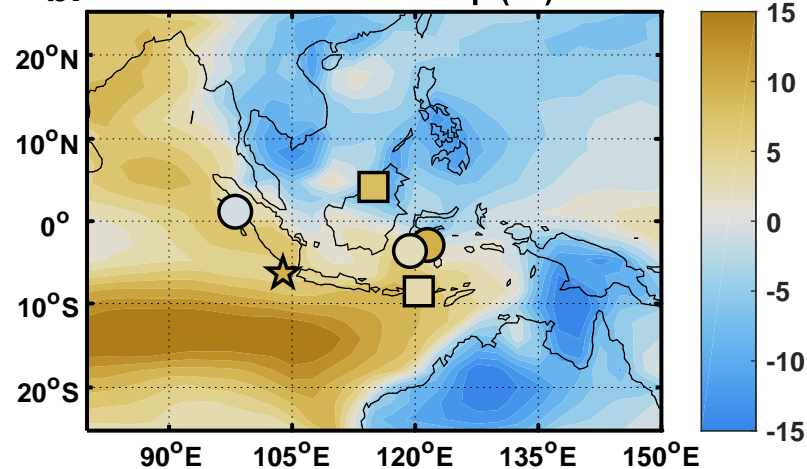




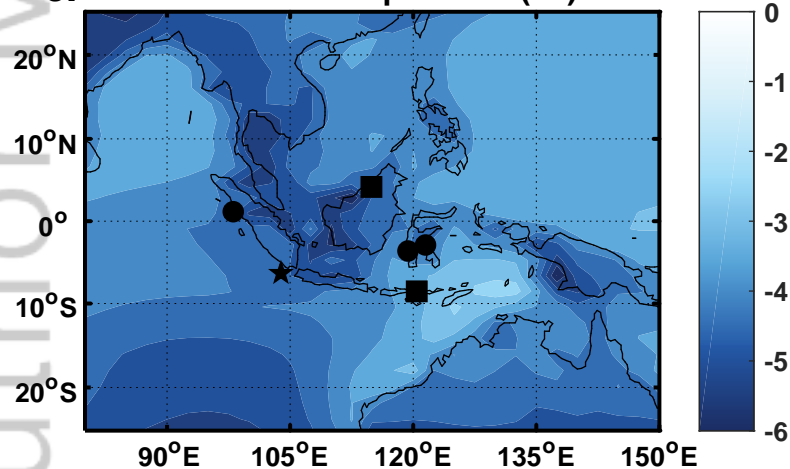
**a. LGM-PI  $\Delta$ Precipitation (mm/day)**



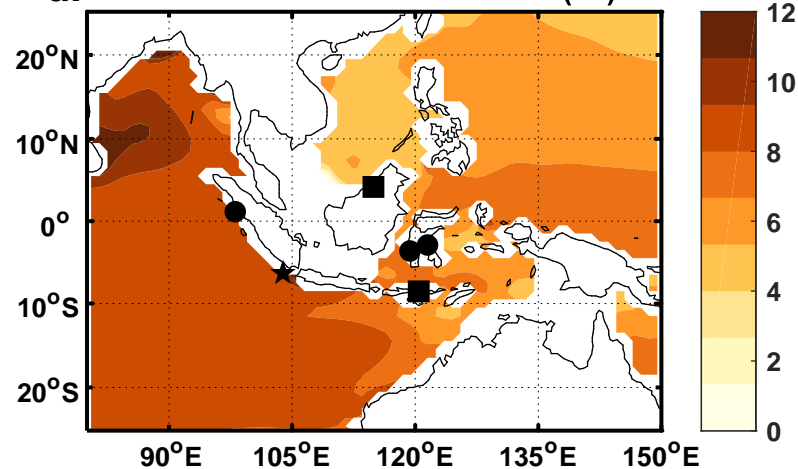
**b. LGM-PI  $\Delta\delta D$  Precip (%)**



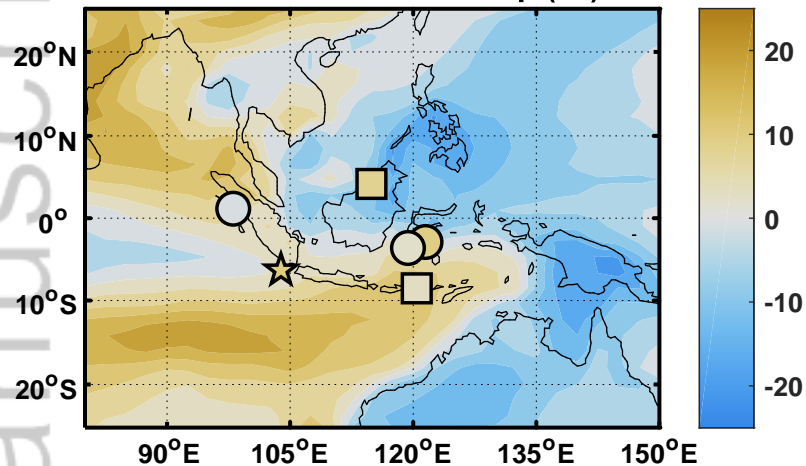
**c. LGM-PI  $\Delta$ Temperature (°C)**



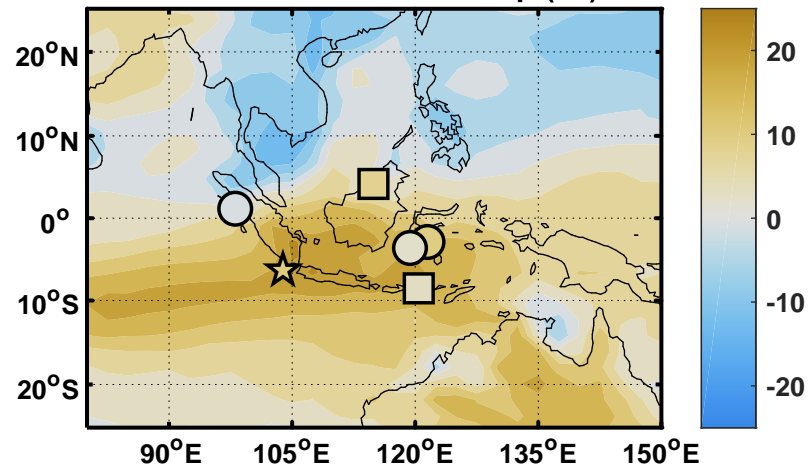
**d. LGM-PI  $\Delta\delta D$  Surface Ocean (‰)**



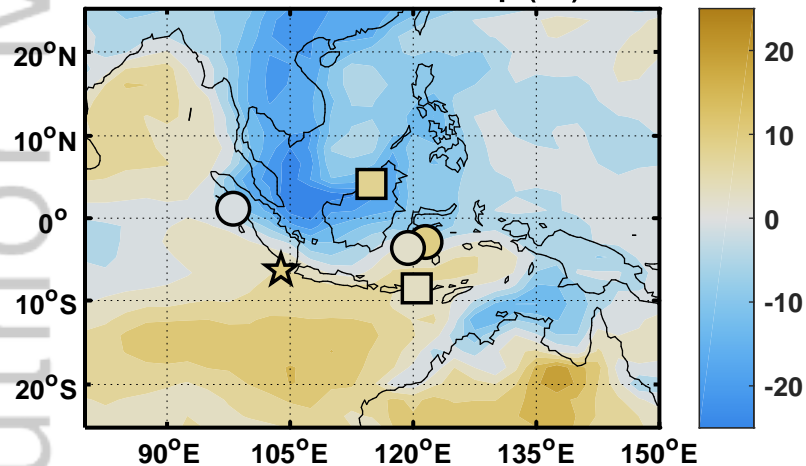
**a. DJFM LGM-PI  $\Delta\delta D$  Precip (‰)**



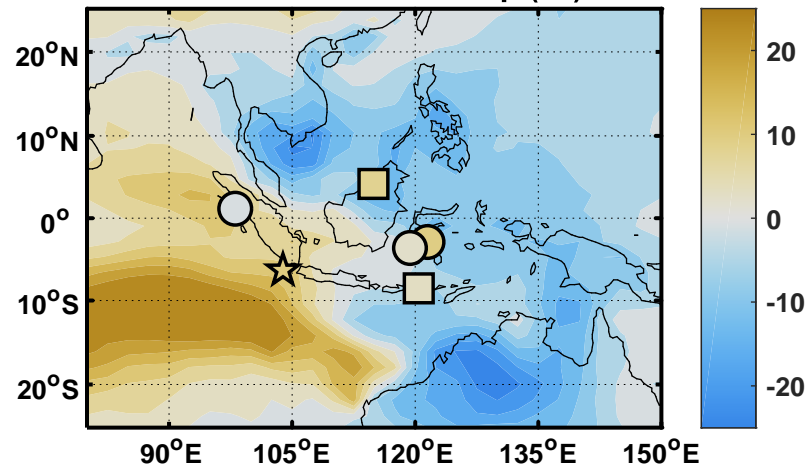
**b. JJAS LGM-PI  $\Delta\delta D$  Precip (‰)**



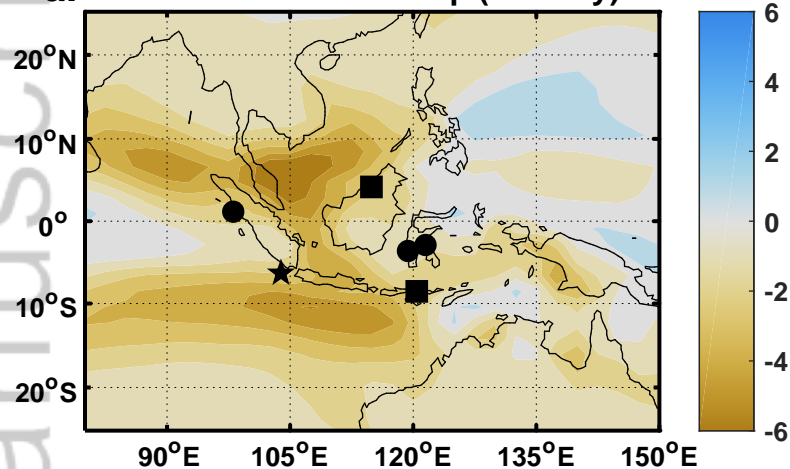
**c. AM LGM-PI  $\Delta\delta D$  Precip (‰)**



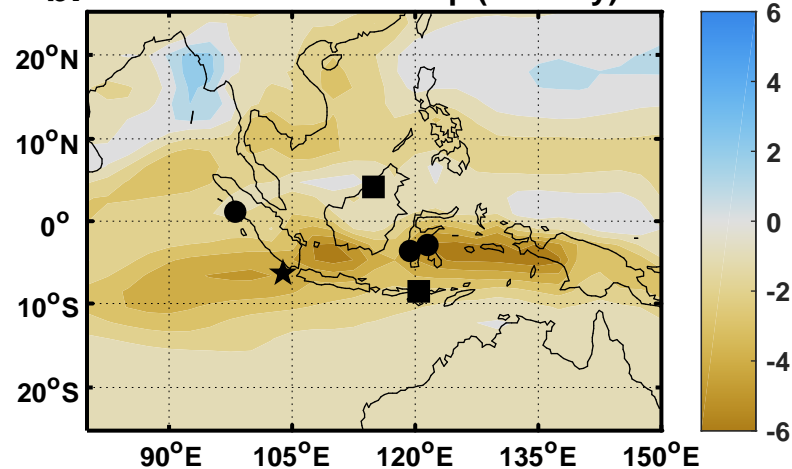
**d. ON LGM-PI  $\Delta\delta D$  Precip (‰)**



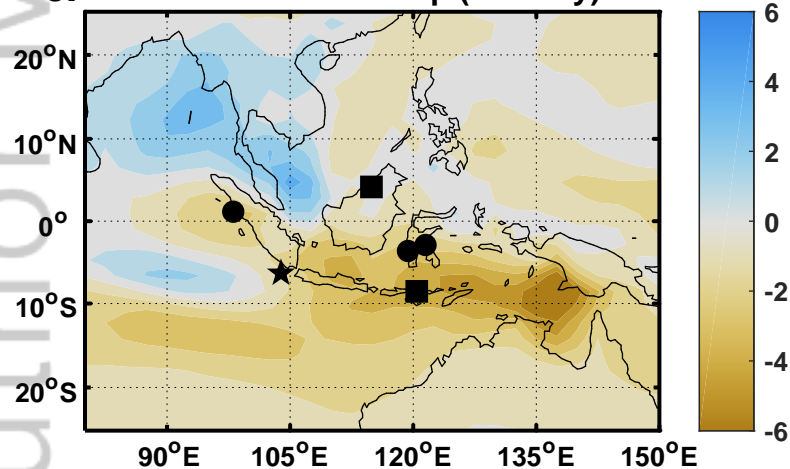
**a. DJFM LGM-PI  $\Delta$ Precip (mm/day)**



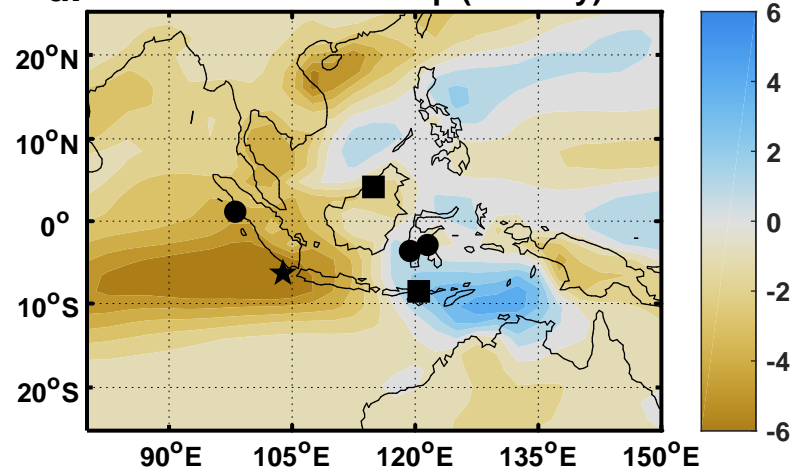
**b. JJAS LGM-PI  $\Delta$ Precip (mm/day)**



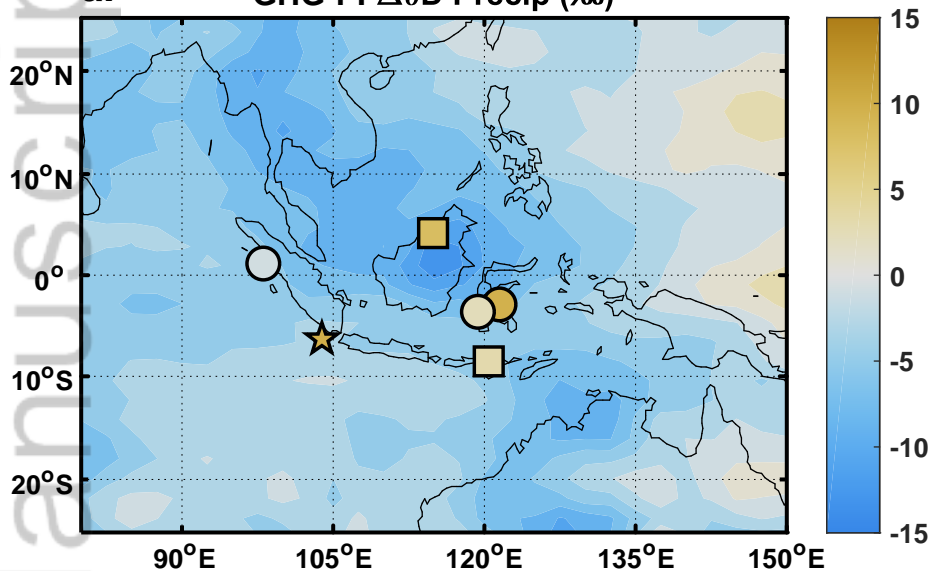
**c. AM LGM-PI  $\Delta$ Precip (mm/day)**



**d. ON LGM-PI  $\Delta$ Precip (mm/day)**



**a. GHG-PI  $\Delta\delta D$  Precip (‰)**



**b. ICE-PI  $\Delta\delta D$  Precip (‰)**

